UDC 533.6.011.55
533.6.071.8
533.6.08

TECHNICAL REPORT OF NATIONAL AERONAUTICAL LABORATORY

TR-37T

Studies of the Flow in a Low Pressure Hypersonic Shock Tunnel Using an Electron-Beam Densitometer

ISAMU WADA

January 1963

NATIONAL AERONAUTICAL LABORATORY

MITAKA, TOKYO, JAPAN

List of NAL Technical Reports

TR- 1	Preliminary Investigatin of N. A. L. Transonic Wind-Tunnel Test-Section	Itu HIRAKI, Takao ISHII & Nobuhiko OSHIMA	Feb. 1960
TR- 2	22.5 MW Main Blower for N. A. L. Transonic Wind Tunnel 1. Performance Test of the Models Blower	Masao YAMANOUCHI, Masakatsu MASTUKI, Jumpei SHIOIRI, & Moriyuki TOMINAGA	May 1960
TR- 3	An Experiment on Angle Measuring Instruments of Airplane Models in Wind Tunnel Test	Yasujiro KOBASHI, Hideo NAGASU Kazuaki TAKASHIMA, & Kiyoshi HAHII	Aug. 1960
TR- 4	Strength of Rotating Discs	Pasuo SATO & Fumio NAGAI	Sept. 1960
TR- 5	Design and Development of N. A. L. 60 cm × 60 cm Transonic Blowdown Wind Tunnel for Flutter Testing	Eiichi NAKAI, Hiroshi HASHIZUME & Yasugaru NAKAMURA	Dec. 1960
TR- 6	Temperature Characteristics of High Temperature Strain Gage	Yukihiko TAKENAKA	Dec. 1960
TR- 7	On the Transonic Test Section	Toshimitsu MURASAKI	Jan. 1961
TR- 8	Preliminary Study for Development of Repeated Load Testing Rigs for Full-Scale Aircraft Structures	Kazuyuki TAKEUCHI & Soshiro IIDA	Mar. 1961
TR- 9	Studies on the Small Disturbance Theory of Transonic Flow (1)	Iwao HOSOKAWA	Mar. 1961
TR-9T	Studies on the Small Disturbance Theory of Transonic Flow (I) —Nonlinear Correction Theory—	Iwao HOSOKAWA	June 1961
TR-10	Cascade Tests of High Stagger Compressor Blades	Masakatsu MASTUKI, Kitao TAKAHARA, Hideo NISHIWAKI & Mitauo MORITA	Mar. 1961
TR-11	Yielding of Rotating Discs of Mild Steel	Yasuo SATO & Fumio NAGAI	Apr. 1961
TR-12	On the Natural Vibration of Thin-Walled Beama of Open Cross Section	Tadahiko KAWAI & Taketoshi HANAWA	May 1961
TR-13	Experimental Results of the Interaction between Shock Wave and Turbulent Boundary Layer	Michiya SUGO & Yukio DENDA	July 1961
TR-14	On Compressible Boundary Layer in Magnetodynamics	Michiya SUGO & Goro OZAWA	July 1961
TR-15	Miniature Pressure Pickups for Measuring the Pressure on Oscillating Airfoils in Supersonic Flow	Takao ISHII & Mitsunori YANAGIZAWA	Aug. 1961
TR-16	On the Difference Method Solutions of the Mixed Boundary Value Problems of Parabolic Partial Differentisl Equations	Kazuo HIGUCHI & Hazime MIYOSHI	Nov. 1961
TR-17	A Theoretical Comment on the Charge-Beam Method of Measuring Gas Density	Isamu WADA, Iwao HOSOKAWA & Hajime MIYOSHI	Dec. 1961
TR-18	Comparison of Inlet Guide V Ane and High Stagger Compressor Blande Performance in a Rotor and in Cascade	Masakatsu MATSUKI	Nov. 1961
TR-19	Strength of High-Speed Rotor	Yasuo SATO & Fumio NAGAI	Dec. 1961
TR-20	A Numerical Method for Solving Blasius' Type Differential Equation	Kazuo HIGUCHI & Hayato TOGAWA	Jan. 1962
TR-21	An Investigation of Two-dimensional Control Surface at Transonic Speed (I)	Nobuhiko KAMIYA	Jan. 1962
TR-22	On the Free Lateral Vibration of a Bean with Variable Cross Section	Tadahiko KAWAI, Hayato TOGAWA & Yoichi HAYASHI	Feb. 1962
TR-23	Monte Carlo Solutions of the Boundary Value Problems for Some Type of Partial Differential Equations	Kazuo HIGUCHI, Toshiyuki TAKAHASHI & Ryozo TORIUMI	Feb. 1962
TR-24	Test Facilities of Turbo-jet Engine Components at N.A.L.	The staff of the Propulsion Division	Feb. 1962
TR-25	Design and Construction of the 2 m × 2 m Transonic Wind Tunnel at the National Aeronautical Laboratory	Vational Aeronautical Laboratory	Mar. 1962

Studies of the Flow in a Low Pressure Hypersonic Shock Tunnel Using an Electron-Beam Densitometer*

By Isamu WADA**

CONTENTS

Summary

The flow of a hypersonic shock tunnel using a double diaphragm is analysed by the method of characteristics in consideration of the growth of the boundary layer in the shock tube and compared with the experimental results measured by an electron-beam densitometer. The density in the test section increases with time according to the boundary layer growth in the medium pressure channel of the shock tunnel and is compared with the computed results of the unsteady flow theory. Some criteria on the effect of the boundary layer and the establishment of the hypersonic flow are given. The density in the boundary layer on a body at a hypersonic speed is also measured by the densitometer.

* Received January 24, 1963
** The First Aerodynamics Division

1. Introduction

The hypersonic shock tunnel, which produces a hypersonic flow of high stagnation pressure and temperature, has been developed for the experiment on the aerodynamic performance of the hypervelocity vehicle and missile[1),2),3)]. The hypersonic shock tunnel with a divergent nozzle has been studied[4),5)]. The reflected type of shock tunnel, which was developed by Prof. F. Tamaki and Dr. C. S. Kim[6)], University of Tokyo, is operated in low pressure.

The Mach number in the test section is determined as a function of the area-ratio, the ratio of the cross-sectional area in the test section to the throat area, and the maximum value of the Mach number is limited by air-liquefaction or air-condensation. It is also controlled by the measurement of the flow, that is, the pressure, temperature and density. When the designed Mach number is high, the static pressure and density of the flow in the test section are low. The instantaneous low-pressure and low-density are not easily measured. In this paper, the density of flow is measured by the electron-beam densitometer designed by the author, instead of by the interferometer.

It is possible that the theory of the unsteady one-dimensional flow is applied to the flow in a low pressure divergent nozzle and the process in the rise of the hypersonic flow in the shock tunnel. The case of the higher pressure has been treated by Prof. Tamaki[5)]. Recently, it has been found that the stagnation state should be estimated by considering the effect of the boundary layer in the medium pressure channel of the tunnel[20)]. In this paper the method of characteristics is applied to the stagnation state, the flow in the throat and the divergent nozzle. The flow condition ahead of the reflected shock is given by Mirels and Braum's theory[19)], and the flow behind the shock gives the stagnation state at the end of the channel. The theoretical results are compared with the following experimental results and the stagnation state determined by the experimental methods of previous papers[7),8)].

The density in the boundary layer on a double wedge is also measured by the electron-beam densitometer in comparison with the density measured by the interferometer.

Details of the designed electron-beam densitometer and the experimental and theoretical results of the hypersonic flow in the two stage shock tunnel are treated in this paper.

2. Equipment

2a. Hypersonic shock tunnel

The schematic diagram of the present shock tunnel and dimensions of the main parts are shown in Fig. 1. High and medium pressure channels are of equal cross-section. The vacuum chamber consists of a test section followed by a straight divergent nozzle and a receiver of large volume. The test section has a rectangular cross-section of $0.30\,\mathrm{m} \times 0.06\,\mathrm{m}$. Each room is separated by cellophane diaphragms. The first diaphragm is broken by the plunger that is driven by solenoid and the second diaphragm by the shock wave advancing in the medium pressure channel. After the reflection of the shock wave, the stagnation state continues for several milliseconds. A strong primary shock will generate in the divergent nozzle and the hypersonic flow will grow in the test section.

The photographs of this shock tunnel are shown in Figs. 2 and 3. Fig. 2 shows the generator of the electron-beam, and Fig. 3, the detector. These instruments will be described in the following section. Fig. 4 shows the Mach-Zehnder interferometer equipped at this tunnel. The pressure of the vacuum chamber is kept below 1 mmHg for this experiment.

2 b. Electron-beam densitometer

The principle and details of this densitometer were described as an absorption method by several authors[9),10),11)]. An electron-beam densitometer has been developed to measure the lower gas density than can be measured by the interferometer. Photographs of the designed densitometer are shown in Figs. 2 and 3. The densitometer consists of the instrument to measure the beam intensity and the electron-beam generator. The density region in this experiment is below about 0.025 kg/m^3. The differential pumping system, whose schematic diagram is shown in Fig. 7, is used, because the pressure of the filament-chamber should be kept below 10^{-4} mmHg for thermal emission from the surface of the filament. It is necessary to place the middle vacuum chamber of about 10^{-2} mmHg between the high vacuum filament chamber and the test section. Chambers communicate with each other through holes. The window holes permit a higher transmission of the electron-beam than metal film such as aluminum foil. Air diffuses from the high pressure side of a hole into the lower pressure chamber and its flow velocity depends upon the air temperature of the higher pressure chamber according to the following equation;

$$V=A\sqrt{\frac{RT}{2\pi\mu}}$$

V: the flow volume per unit time
A: the hole area
T: the temperature of higher pressure chamber
R: Gas constant
μ: the molecular weight of air

This value must be considered in choosing the capacity of vacuum pumps which are shown in Fig. 7.

Two holes and the filament must be adjusted on a straight line. The scintillation probe also should be located in the center line of the electron-beam. The mechanism of this instrument is designed as is shown in Fig. 6. The instrument for the source of the electron-beam is made of an electron-gun, a part of an electron microscope, which is manufactured by Akashi Seisakusho Ltd.

The block diagram of the system to measure the intensity of the electron-beam, made by Rigaku Denki Co., Ltd., is shown in Fig. 8. The total energy of the electron-beam is transferred to photons by a phosphor. The phosphor is a solid substance, composed of organic fluor and a transparent plastics, made by Matsushita Electric Works, Ltd. The output current of the photomultiplier corresponds with the intensity of the electron-beam. This output which is converted into voltage by a resistance is connected with a synchroscope (DS-5155, Iwasaki Communication Apparatus Co. Ltd.) through a D. C. amplifier (SD-20-DA, Iwasaki C. A.

Co. Ltd.) as is shown in Fig. 8.

The schematic diagram of this densitometer is shown in Fig. 6. The result of calibration is shown in Fig. 9.

The electron-beam densitometer has been used for the experiment of the low pressure shock tube[15),16)], and electron shadowgraphs and afterglow pictures[10)], and another method using an electron-beam fluorescence probe have been developed[13),14)].

2c. Piezo-electric pressure gauge and thin film thermometer

The stagnation condition of this shock tunnel is determined by the piezo-electric pressure gauge using barium titanate, and by the thin film thermometer. These gauges were described in previous papers[7),8)]. The pressure gauge using barium titanate is shown in Appendix D and calibrated by the method described in one of the previous papers. The increasing pressure of stagnation is observed by this gauge.

3. The flow in a hypersonic shock tunnel with a divergent nozzle

3a. Theoretical treatment for an unsteady flow in a duct

The flow through the duct of the variable cross-sectional area is treated by the following unsteady quasi-one dimensional differential equations[17)].

The equation of continuity;

$$\frac{1}{\rho}\frac{\partial \rho}{\partial t}+\frac{u}{\rho}\frac{\partial \rho}{\partial x}+\frac{\partial u}{\partial x}=-\frac{u}{A}-\frac{1}{A}\frac{\partial A}{\partial t} \tag{3.1}$$

The equation of motion;

$$\frac{\partial u}{\partial t}+u\frac{\partial u}{\partial x}\equiv\frac{du}{dt}=-\frac{1}{\rho}\frac{\partial P}{\partial x} \tag{3.2}$$

The entropy is considered as constant along the path of a gas particle;

$$\frac{\partial s}{\partial t}+u\frac{\partial s}{\partial x}=0$$

and

$$(\gamma-1)T\frac{ds}{dt}=\frac{1}{\rho}\frac{dP}{dt}-\frac{a^2}{\rho}\frac{d\rho}{dt}=0 \tag{3.3}$$

for a perfect gas.

Substituting the above relation to equation (3.1) multiplied by a^2,

$$\frac{1}{\rho}\frac{dP}{dt}+a^2\frac{\partial u}{\partial x}=-a^2\left(\frac{u}{A}\frac{\partial A}{\partial x}+\frac{1}{A}\frac{\partial A}{\partial t}\right) \tag{3.4}$$

Adding and subtracting the momentum equation multiplied by a, from this equation,

$$\pm a\left(\frac{du}{dt}\pm a\frac{\partial u}{\partial x}\right)+\frac{1}{\rho}\left(\frac{dP}{dt}\pm a\frac{\partial P}{\partial x}\right)=-a^2\left(\frac{u}{A}\frac{\partial A}{\partial x}+\frac{1}{A}\frac{\partial A}{\partial t}\right)$$

The rate of change of the unknown functions along characteristic directions;

$$\left.\begin{aligned}\left(\frac{\partial u}{\partial t}\right)_{x+at}+\frac{1}{\rho a}\left(\frac{\partial P}{\partial t}\right)_{x+at}&=-a\left(\frac{u}{A}\frac{\partial A}{\partial x}+\frac{1}{A}\frac{\partial A}{\partial t}\right)\\ -\left(\frac{\partial u}{\partial t}\right)_{x-at}+\frac{1}{\rho a}\left(\frac{\partial P}{\partial t}\right)_{x-at}&=-a\left(\frac{u}{A}\frac{\partial A}{\partial x}+\frac{1}{A}\frac{\partial A}{\partial t}\right)\end{aligned}\right\} \tag{3.5}$$

and equation (3.3) contains the total derivative of entropy along the direction, $u=dx/dt$. The terms of the area change depending upon time in the above equations (3.5) are eliminated.

$$\left.\begin{aligned}\frac{du}{a_0}+e^{\frac{s-s_0}{2c_p}}d\left\{\frac{2}{\gamma-1}\left(\frac{P}{P_0}\right)^{\frac{\gamma-1}{2\gamma}}\right\}&=-\frac{a}{a_0}\left(\frac{u}{a_0}\frac{1}{A}\frac{\partial A}{\partial x}\right)d(a_0t)\\ -\frac{du}{a_0}+e^{\frac{s-s_0}{2c_p}}d\left\{\frac{2}{\gamma-1}\left(\frac{P}{P_0}\right)^{\frac{\gamma-1}{2\gamma}}\right\}&=-\frac{a}{a_0}\left(\frac{u}{a_0}\frac{1}{A}\frac{\partial A}{\partial x}\right)d(a_0t)\end{aligned}\right\}\qquad(3.6)$$

In the case of constant area, the right hand sides of the equations (3.6) disappear and entropy should be constant.

$$\left.\begin{aligned}\frac{du}{a_0}+d\left\{\frac{2}{\gamma-1}\left(\frac{P}{P_0}\right)^{\frac{\gamma-1}{2\gamma}}\right\}&=0\\ -\frac{du}{a_0}+d\left\{\frac{2}{\gamma-1}\left(\frac{P}{P_0}\right)^{\frac{\gamma-1}{2\gamma}}\right\}&=0\end{aligned}\right\}\qquad(3.7)$$

3 b. Constant area shock tunnel[18]

When the diaphragm, which separates the high and the medium pressure channels, is ruptured, the rarefaction wave is propagated into the high pressure channel and the plane shock moves ahead of the contact surface in a direction opposite to the rarefaction wave as shown in Fig. 10. The contact surface behaves like the piston that has attained the velocity equal to the velocity of gas particles. The flow model is determined from the characteristic equations (3.7) and the shock relations, that is, the theory of the ordinary shock tube.

As the result of the boundary layer growth behind the incident shock W_1, the conditions ahead of the reflected shock W_2 are given in Appendix E[19]. The conditions behind the reflected shock are determined by the characteristic equations as shown in Fig. 11, on the basis of the fact that the flow at the throat should be sonic and M_5 at the end of tube can be calculated as the function of A_5/A_* (eq. (3.8)). In region 5, the characteristics in the wave diagram are given by the straight lines having $u_5\pm a_5$. The flow condition at the end of the shock tube given by the above wave diagram determines the stagnation condition of the hypersonic shock tunnel. The stagnation state and the throat conditions vary slightly with time. It has been found by Rudinger that the pressure-rise is considerably magnified by the reflected shock W_2 from the end of shock tube[20].

The computing process of Region 5 is shown in Appendix C. The velocity of the reflected shock, W_2 and that of the shock reflected from the contact surface, W_3 vary with time, too. The initial stagnation conditions of the hypersonic shock tunnel and the initial throat conditions determined by theory are shown in Table 1, when the initial pressure ratios are 10, 12 and 14.

3 c. The discontinuous change of the cross-sectional area of shock tubes[18]

The relations of isentropic flow in a discontinuous cross-sectional area are assumed as follows;

$$\left.\begin{aligned}A_5/A_*&=\frac{1}{M_5}\left\{\frac{2+(\gamma-1)M_5^2}{\gamma+1}\right\}^{\frac{\gamma+1}{2(\gamma-1)}}\\ P_5/P_*&=\left\{\frac{\gamma+1}{2+(\gamma-1)M_5^2}\right\}^{\frac{\gamma}{\gamma-1}}\\ T_5/T_*&=\left(\frac{\gamma+1}{2}\right)\Big/\left(1+\frac{\gamma-1}{2}M_5^2\right)\end{aligned}\right\}\qquad(3.8)$$

$$\rho_5/\rho_* = \left\{\left(\frac{\gamma+1}{2}\right)\Big/\left(1+\frac{\gamma-1}{2}M_5^2\right)\right\}^{\frac{1}{\gamma-1}} \qquad \Big|$$

As A_5/A_* is constant, M_5, the flow Mach number in the stagnation of the shock tunnel is known. The stagnation conditions, P_5, T_5 and ρ_5 are determined from the above equations and the particle velocity at the throat of the shock tunnel should be sonic.

The relations of the flow in the shock tube, the cross-sectional area of which is constant, are treated by equations (3.7) and Appendix E. The expansion fans added to the particle velocity $u=a_*$ that varies slightly with time by the effect of the boundary layer, are described as shown in Fig. 12 and the quantities of the inlet flow in a divergent nozzle are given.

3 d. Analysis of the flow in a divergent nozzle by the method of characteristics

The equations (3.6) are calculated from the initial conditions which are fixed in the proceeding chapter 3 c. This numerical calculation is done by an electric digital computer, Burrough 205 at National Aeronautical Laboratory. The process of this calculation is shown in Appendix B. Fig. 13 shows a typical wave diagram for a divergent channel of $M=6.5$, when the flow behind the primary shock is supersonic at the inlet of the divergent part. The diagram shows that the primary shock weakens gradually as it propagates through the divergent nozzle, the contact surface (the entropy discontinuity) advances behind it, and the secondary shock appears behind the contact surface.

In Figs. 19, 20 and 21, the flow Mach number, pressure and density at $x=0.55$ m are plotted against a_*t, respectively. The difference between the steady flow and the modified ideal flow shows the accuracy of this calculation using the method of characteristics. This accuracy depends upon the intervals between the characteristic curves in the wave diagram. When the intervals are a half and a quarter of this calculation, the flow Mach number of the modified ideal flow approaches to 6.47 and 6.50, respectively. More detailed results of the accuracy will be discussed by H. Miyoshi, National Aeronautical Laboratory. It is assumed in the modified ideal flow case that the stagnation state, when the attenuating incident shock by the boundary layer effect is reflected from the end of medium pressure channel, would be kept constant for the duration of the shock tunnel.

4. Experimental results

The typical performance of the hypersonic shock tunnel is shown in Fig. 14 a. The upper curve represents the density variation in the test section measured by the designed electron-beam densitometer and the lower curve represents the variation of stagnation temperature measured by the thin film thermometer. It is shown that the variation of stagnation temperature is not large in comparison with pressure. Fig. 14 b shows the stagnation pressure measured by the piezo-electric pressure gauge which can be compared with the theory in Fig. 18. The pressure behind the reflected shock increases gradually with time as a result of the boundary layer growth in the medium pressure channel.

The variations of density in the test section are shown in Figs. 15a, 15b and 15c, in the cases of the initial pressure ratios 10, 12 and 14, respectively. The density jumps when the

primary shock and the contact surface arrive at the test section, and decreases with the secondary shock. After that the density increases gradually with time as predicted by the theory.

The typical photograph of the first shock using the Mach-Zehnder interferometer is shown in Fig. 16. It is not possible to determine the shock strength in this tunnel because the variation of density is too small.

The experimental result of the shock Mach number is compared with the theoretical one given by the ideal shock tube theory, in Fig. 17 a. It is shown that the experimental values disagree with the theory by the attenuation of the shock wave. The pressure and temperature behind the reflected shock are calculated from the shock Mach number using the normal shock relations and these experimental values are compared with the ideal shock tube theory, in Fig. 17 b.

In the cases of lower initial pressures in the high and the medium pressure channels and the pressures of the vacuum chamber of 0.7 mmHg, the variations of density with time in the test section are also measured. These results are shown in Fig. 22. The increasing gradients of density against $a_* t$ are smaller than the gradient in the case of $P_2=12$ ata and $P_1=1$ ata. When $P_2=4$ata and $P_1=1/3$ ata, the density is considered almost constant for about 1 m sec because the absolute value of density is too small. When $P_2=3$ ata and $P_1=1/4$ ata, the establishment of the hypersonic flow in the test section is not expected as is presented by Curve C of Fig. 22.

The variation of density with time is also measured at the several points near a double-wedge and a flat-nosed cylinder, whose positions are shown in Figs. 23 and 24, respectively. When $P_2=4$ ata, $P_1=1/3$ ata and $P_{vac}=0.6\sim0.7$ mmHg, the increase of density can be neglected as is presented in Fig. 22. The establishment of the hypersonic flow is shown in Figs. 21 and 22 and the time necessary for the establishment is about 0.25 m sec. In the boundary layer on the forward and backward surface of the double-wedge, about 0.6 m sec is needed to get the steady state. This time is greater than that of free stream and that of the flow behind the shock attached to the leading edge of aerofoil.

It is also shown from these experimental results that some periodic vibration of density is in the boundary layer and has a fundamental frequency of 10 kc and the higher order. This vibration is not observed in the free stream of $M=6.5$. In the wake of the bodies flying at hypersonic speeds, the effect of the boundary layer on the forward surface of the double-wedge seems to exist. In the case of an axial symmetrical body (flat-nosed cylinder), the fluctuation of the density is observed as shown in Fig. 24.

The distribution of the density around the double-wedge at $M=6.5$ is observed by using the interferometer as shown in Fig. 23, and the density measured by the electron-beam densitometer is shown in Fig. 26. These results are compared with the density obtained from the shock-expansion theory in Fig. 25.

5. Comparison between computed and observed data

The variation of the stagnation state, especially, stagnation pressure is shown in Fig. 14 b and compared with the computed results by the method of characteristics in consideration of the boundary layer effect behind the incident shock W_1 in Fig. 18. The experimental results of pressure should be observed between the laminar boundary layer case and turbulent case, and are estimated to agree with the turbulent boundary layer case in order to deal with the performance of the shock tunnel.

The computed Mach number, pressure and density at $x=0.55$ m are shown in Figs. 19, 20 and 21, and show the differences of the unsteady modified ideal flow, the unsteady flow considering the non-stationary stagnation (by the effect of the turbulent boundary layer) and the steady flow having $M=6.5$ at $x=0.55$ m. The difference between the stationary part of the modified ideal flow and the steady flow shows the accuracy of calculation, and depends upon the interval of Mach lines in the wave diagram. The unsteady parts of this calculation (first shock, contact surface and secondary shock) are done more exactly because a smaller interval than the stationary part is used in this region. The non-uniformity after the secondary shock is caused by the variation of the stagnation state.

In Fig. 21, the variation of the theoretical density with time is compared with the experimental results which are shown in Fig. 15 a. The theoretical result of the turbulent boundary layer case agrees with the observed data except the region from the contact surface to the secondary shock. The disagreement in this region is caused by the fact that the ratio of the specific heats for air is assumed to be constant in the theoretical treatment.

The above comparison between the computed and experimental results shows that the performance of the two-stage hypersonic shock tunnel is able to be determined in consideration of the turbulent boundary layer.

6. Conclusions

The conclusions from the above theoretical and experimental study are shown below:

1. The Mach number of the low pressure shock tunnel can be determined by the theory of unsteady one-dimensional isentropic flow, by which the Mach number, the function of area ratio, is given. The flow Mach number of the tunnel is 6.5, where the area ratio is 75.

2. The stagnation pressure of the shock tunnel are about 6~10% lower than the pressure at the closed end of shock tube when the initial pressure ratio is the same. The pressure increases slightly with time as the result of the boundary layer growth in the medium pressure channel and is evaluated in consideration of the turbulent boundary layer.

3. The density at the test section increases slightly with time. The experimental result of density from the contact surface to the secondary shock is smaller than the theoretical prediction. It seems that this discrepancy depends upon the assumption of the ratio of the specific heats for air, because the temperature in a part of this region is below the critical one of air-liquefaction.

4. It is not necessary in the region of this experiment to consider the laminar boundary layer part, in order to treat the effect of non-uniformity in the medium pressure channel on the performance of the hypersonic shock tunnel. The transition time of the boundary layer behind the incident shock is about 90 μ sec.

5. The variation of density of the free stream in the test section is neglected when the initial pressures in the high and the medium pressure channels are 4 ata and 1/3 ata, respectively. The establishment of the hypersonic flow in the test section is not expected below these pressures when the pressure of the vacuum chamber is 0.7 mmHg.

6. The designed electron-beam densitometer is more available to measure lower density than this experiment. The hypersonic shock tunnel will be operated at a lower pressure than this experiment and used for the aerodynamic studies of bodies flying at hypersonic speeds and of the periodic vibration of the density in the boundary layer on their surface and in the wake.

7. Acknowledgement

The author would like to express his sincere appreciation to Prof. F. Tamaki, University of Tokyo, for his competent advice in the present study.

The author is also grateful for the assistance in this project expressed by Mr. R. Matsuzaki, Mr. K. Soga and Mr. R. Saito, National Aeronautical Laboratory, and for the programming of the calculation done by Mr. H. Miyoshi, National Aeronautical Laboratory.

The author is also indebted to Mr. Tochigi, Mr. Satsuka, Akashi Seisakusho Ltd. and Mr. Kariya, Rigaku Denki Co. Ltd. for their help in construction of the electron-beam densitometer.

References

1) I. I. Glass & J. G. Hall: Shock Tubes, UTIA Review, No. 12, May 1958 & NAVORD Report 1488, Vol. 6, 1959.
2) A. R. Collar & J. Tinkler: Hypersonic Flow, (Butterworths Scientific Publications, London, 1960).
3) A. Ferri: Fundamental Data obtained from Shock-Tube Experiments, (Pergamon Press, 1961).
4) A. Hertzberg: A Shock Tube Method of Generating Hypersonic Flows, Jour. Aero. Sci., Vol. 18, No. 12, pp. 803-804, Dec. 1951.
5) F. Tamaki: A Divergent Shock Tube for Obtaining Supersonic Flows, Jour. Phys. Soc. Japan, Vol. 11, No. 4, pp. 434-439, April 1956.
6) F. Tamaki & C. S. Kim: Studies on the Hypersonic Flow Using a Double-Diaphragm Shock Tube, Jour. Phys. Soc. Japan, Vol. 12 No. 5, pp. 550-555, May 1957.
7) I. Wada & R. Matsuzaki: Calibration of Piezo-electric Pressure Gauge by Using Shock Tube, Jour. Japan Soc. Aero. Sci., Vol. 9, No. 2, pp. 62-63, Feb. 1961 (in Japanese).
8) I. Wada & R. Matsuzaki; Heat Gauge Records on Shock Tube End-Plate, Jour. Japan Appl. Phys., Vol. **1**, No. 1, pp. 65-66, July 1962.
9) V. E. Schopper & B. Schumacher: Messung von Gasdichten mit Korpuskularstrahlsonden, Z. Naturforsch. **6a**, pp. 700-705, 1951.
10) A. E. Grün, E. Schopper & B. Schumacher: Electron Shadowgraphs and Afterglow Pictures of Gas Jets at Low Densities, Jour. Appl. Phys., Vol. 24, No. 12, pp. 1527-1528, Dec. 1953.
11) I. Wada: Electron-beam Densitometer, Jour. Japan Soc. Vacuum, Vol. 3, No. 5, pp. 165-168, May 1960 (in Japanese).

12) F. C. Hurlbut: Rarefied Gas Dynamics (Proceedings of the First International Symposium held at Nice) ed., by F. M. Devienne (Pergamon Press, 1960) 55 p.
13) B. W. Schumacher & E. O. Gadamer: Electron Beam Fluorescence Probe for Measuring the Local Gas Density in a Wide Field of Observation, Can. Jour. Phys., Vol. 36, No. 6, pp. 659-671, June 1958.
14) E. O. Gadamer: Measurement of the Density Distribution in a Rarefied Gas Flow Using the Fluorescence Induced by a Thin Electron Beam, UTIA Report, No. 80, March, 1962.
15) D. Venable & D. E. Kaplan: Electron Beam Method of Determining Density Profiles across Shock Waves in Gases at Low Densities, Jour. Appl. Phys., Vol. 26, No. 5, pp. 639-640, May 1955.
16) R. E. Duff: Shock-Tube Performance at Low Initial Pressure, Phys. Fluids, Vol. 2, No. 2, pp. 207-216, March-April 1959.
17) K. Oswatitsch: Gasdynamik (Springer Verlag, Vienna, 1952) 127 p, or Gas Dynamics (Academic Press, New York, 1956) 163 p.
18) I. I. Glass, W. Martin & G. N. Patterson: A Theoretical and Experimental Study of the Shock Tube, UTIA Report No. 2, Nov. 1953.
19) H. Mirels: Attenuation in a Shock Tube Due to Unsteady-Boundary Layer Action, NACA TN-3278, Aug. 1956.
H. Mirels & W. H. Braun: Nonuniformities in Shock-Tube Flow Due to Unsteady-Boundary-Layer Action, NACA TN 4021, May 1957.
20) G. Rudinger: Effect of Boundary-Layer Growth in a Shock Tube on Shock Reflection from a Closed End, Phys. Fluids, Vol. 4, No. 12, pp. 1463-1473, Dec. 1961.

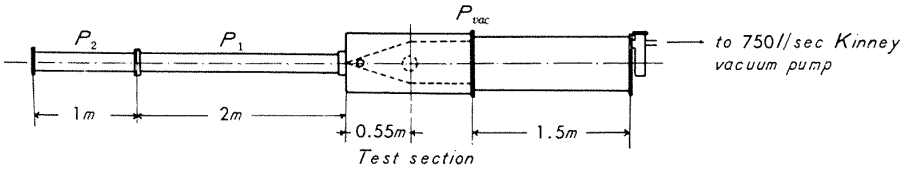

P_1: High pressure channel P_1: Medium pressure channel
P_{vac}: Vacuum chamber

Fig. 1. Schematic diagram of hypersonic shock tunnel.

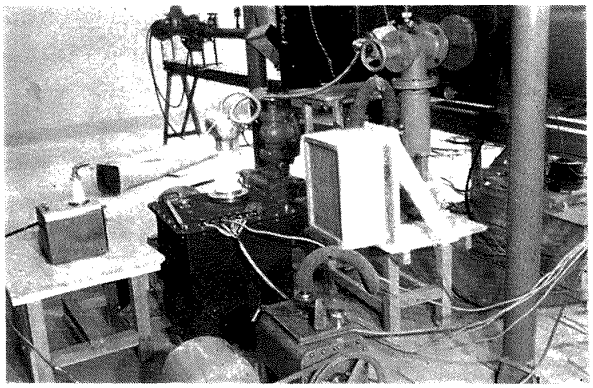

Fig. 2. Electron-beam generator mounted on the side wall of shock tunnel.

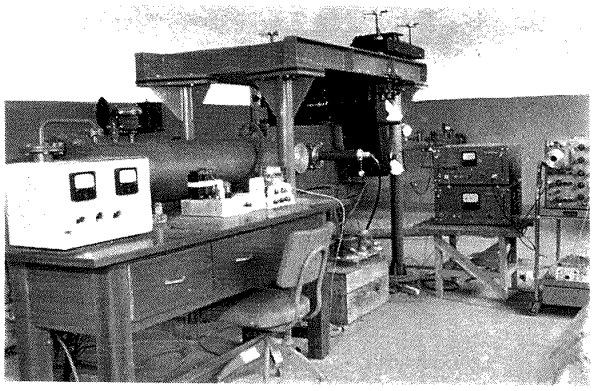

Fig. 3. The instrument to measure the intensity of electron-beam.

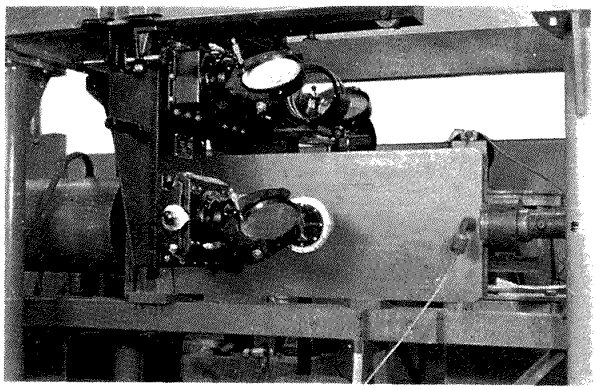

Fig. 4. The test section of shock tunnel and the 15 cm diameter Mach-Zehnder interferometer.

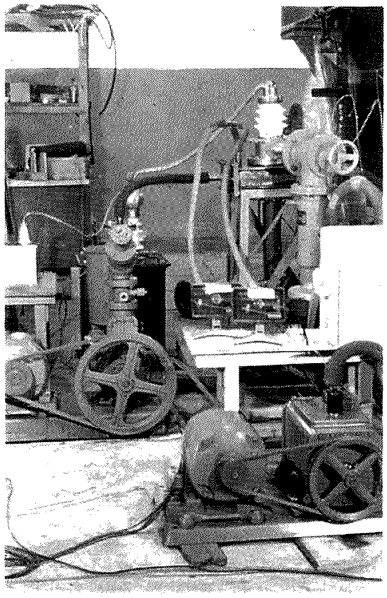

Fig. 5. Arrangement to calibrate electron-beam densitometer.

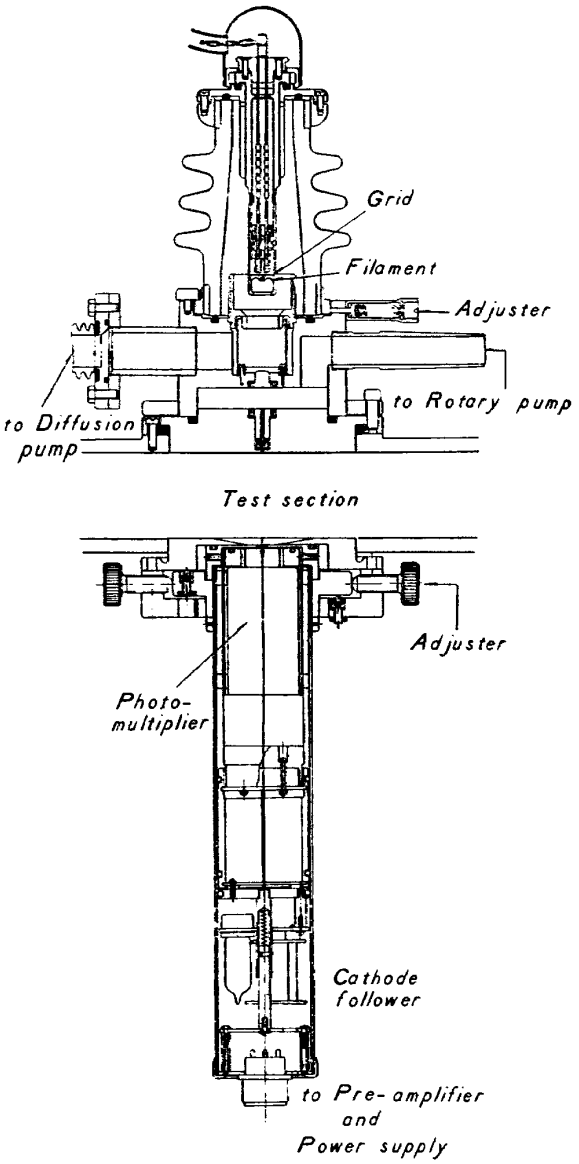

Fig. 6. Arrangement of electron-beam densitometer mounted on the wall of shock tube.

Plate voltgae 0～−30 kV
Grid voltage 0～100 V
Filament voltage 0～1 V.A.C.

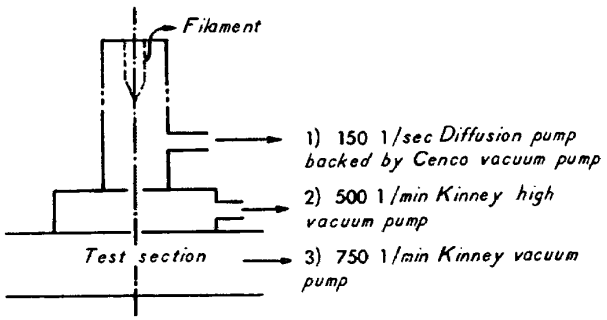

Fig. 7. Differential pumping system of electron-beam densitometer.

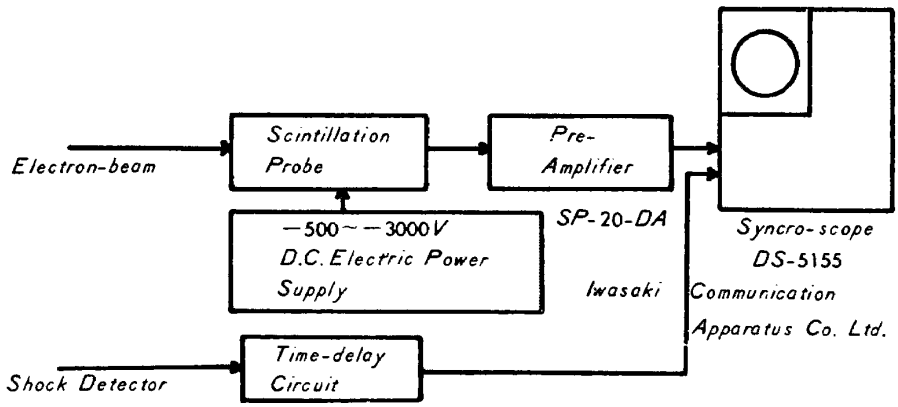

Fig. 8. Block diagram of system for the measurement of intensity of electron-beam.

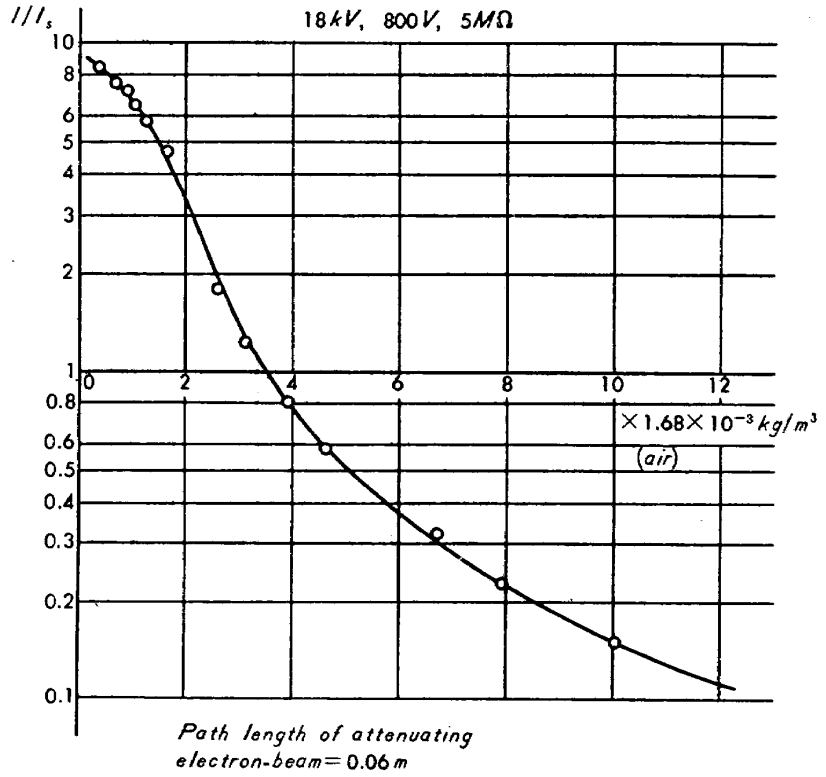

Fig. 9. Result of calibration of electron-beam densitometer.

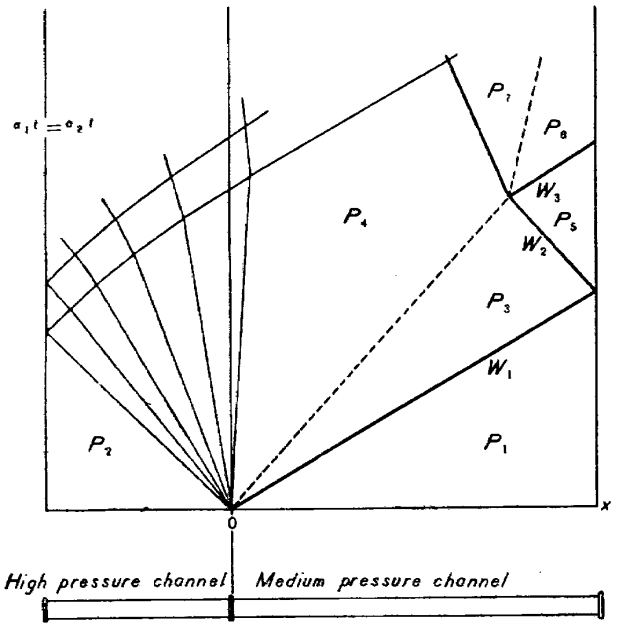

Fig. 10. Theoretical diagram of (x, at)-plane showing the waves and states in the high and medium channels.

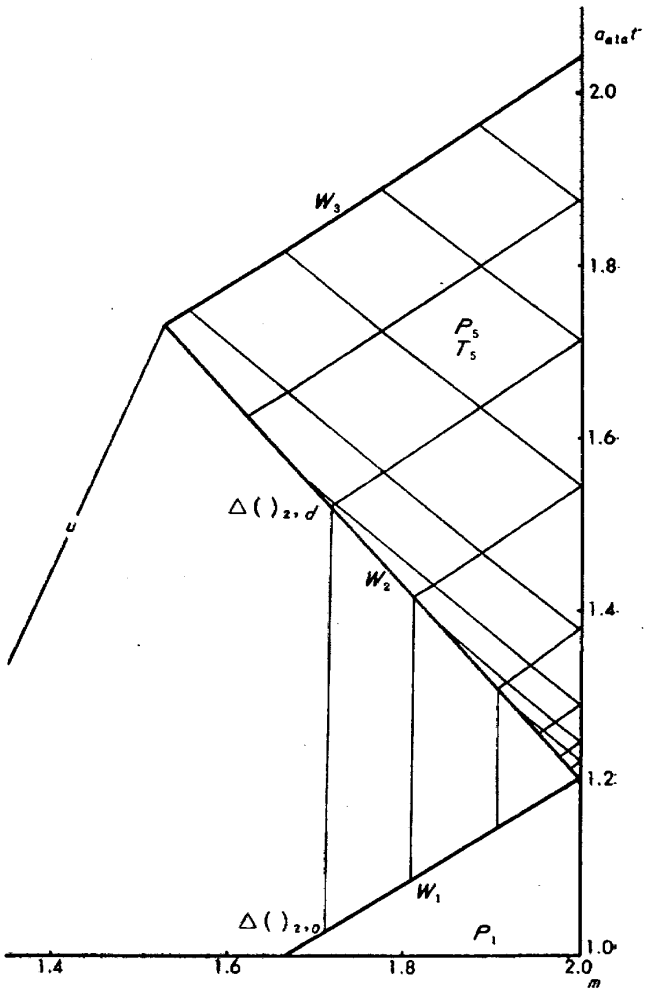

Fig. 11. Wave diagram in region 5 (stagnation state).

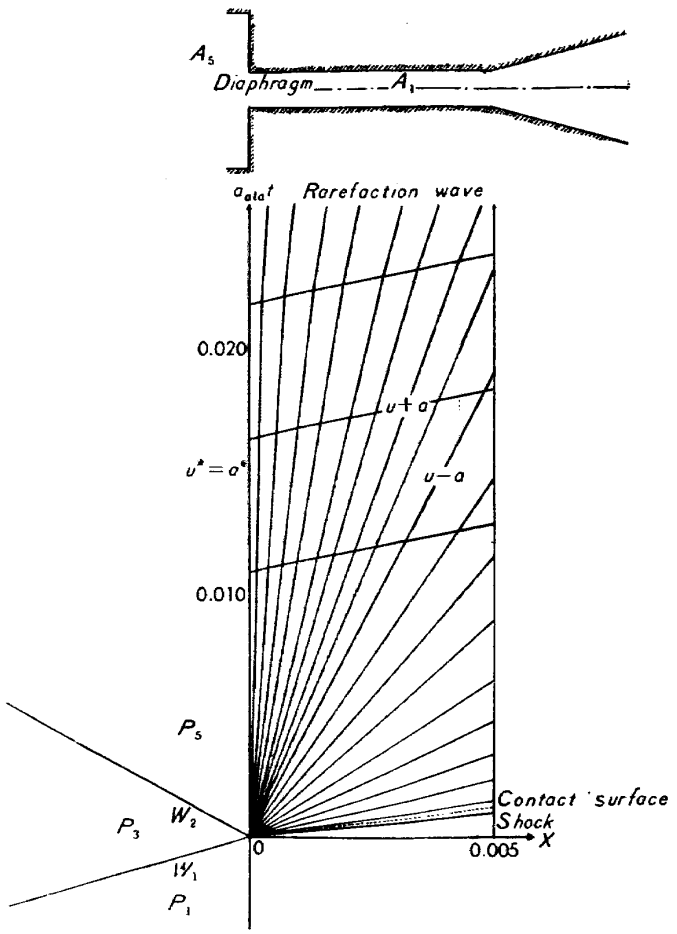

Fig. 12. Wave diagram in the throat.

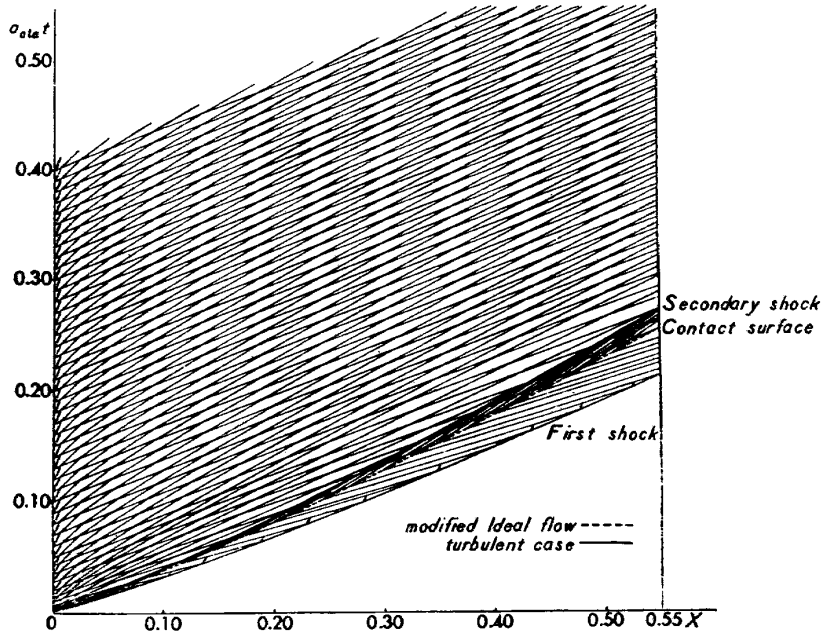

Fig. 13. Wave diagram for the divergent nozzle when the initial pressure ratio, $P_2/P_1=12$.

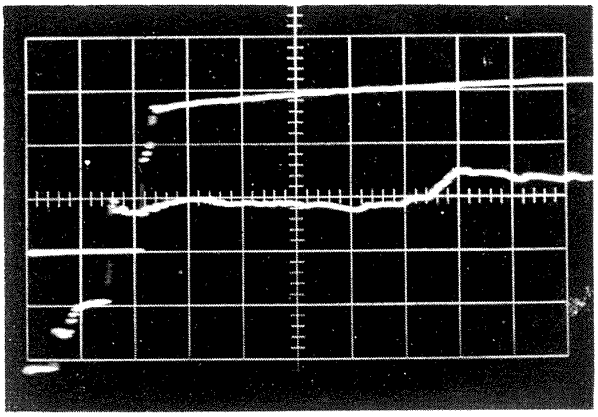

500 μ sec./division, $P_2/P_1=12$
upper record; density in test section, 5V/division
lower record; wall temperature at stagnation
0.1V/division

Fig. 14 a. The performance of shock tunnel.

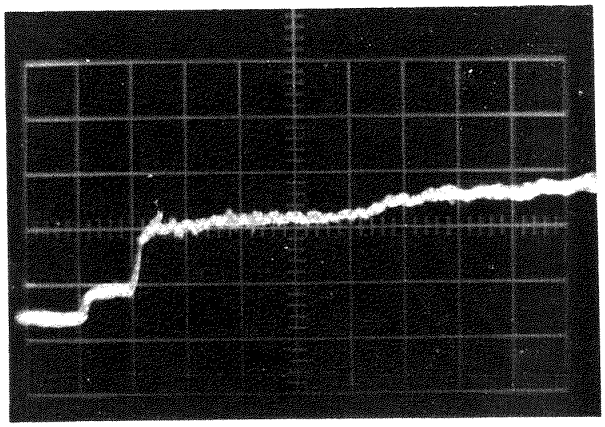

500 μ sec./division, $P_2/P_1=12$
0.1V/division

Fig. 14 b. Variation of stagnation pressure measured by piezo-electric pressure gauge (barium-titanate).

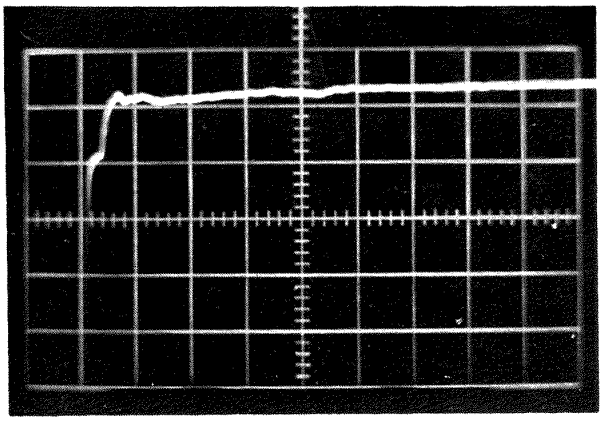

I) 200 μ sec./division 1V/division

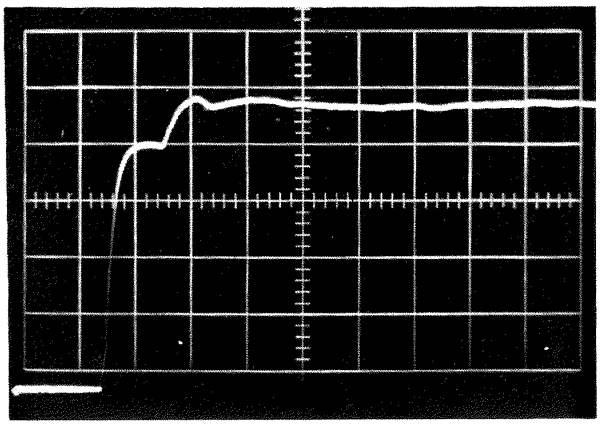

II) 100 μ sec./division 2V/division

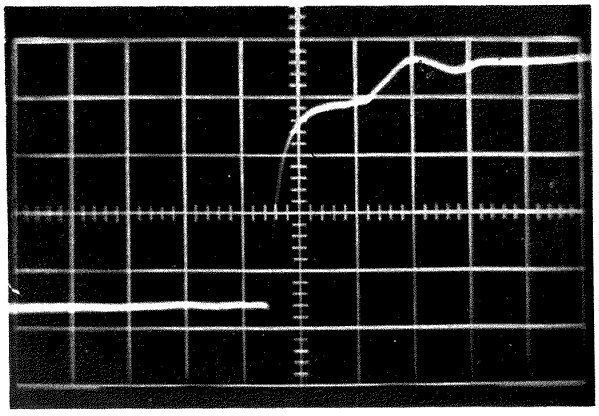

III) 50 μ sec./division 1V/division

Fig. 15 a. Variation of density in test section; initial pressure ratio, $P_2/P_1=12$.

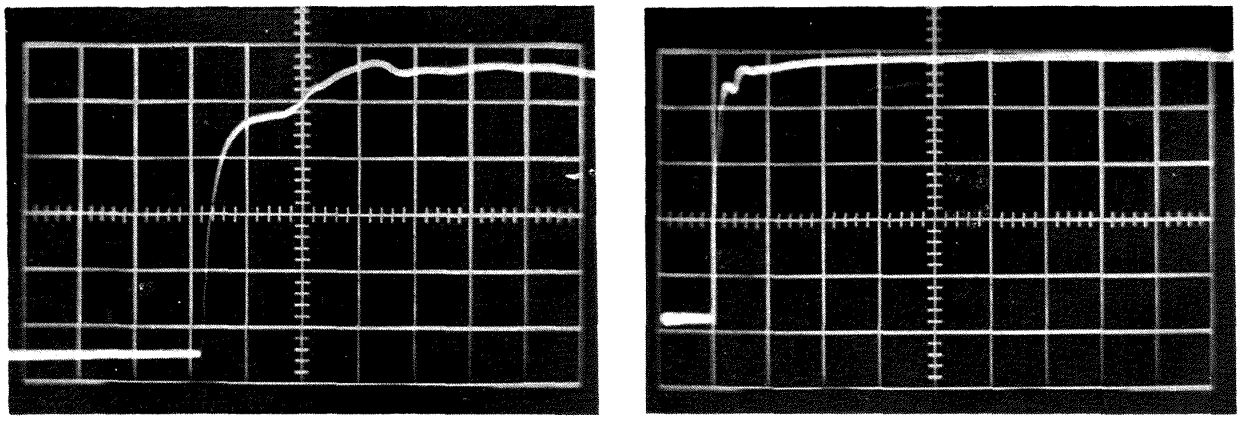

50 μ sec./division 2V/division　　200 μ sec./division 2V/division

Fig. 15 b. Varation of density in test section; initial pressure ratio, $P_2/P_1=14$.

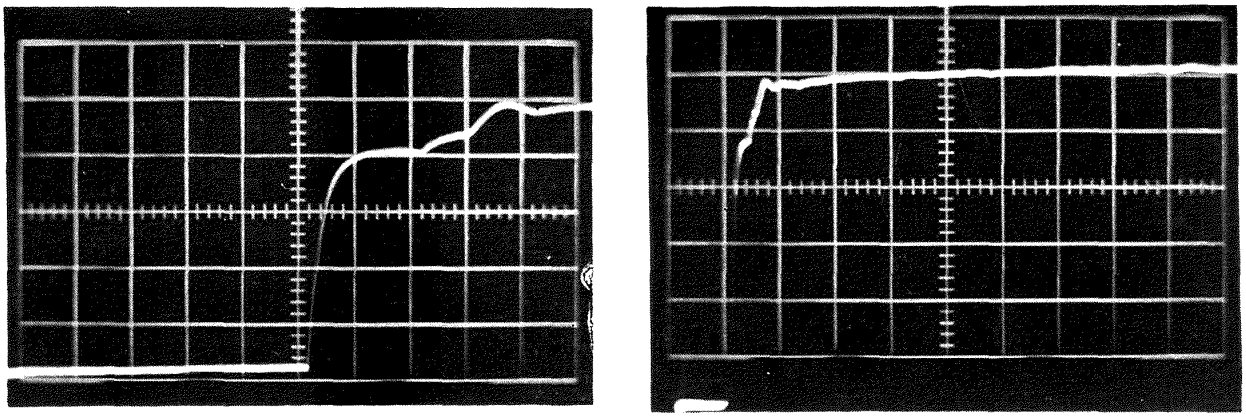

50 μ sec./division 1V/division　　200 μ sec./division 2V/division

Fig. 15 c. Variation of density in test section; initial pressure ratio, $P_2/P_1=10$.

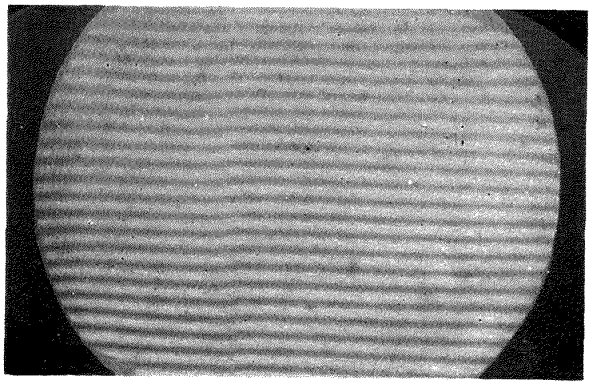

Fig. 16. First shock observed by Mach-Zehnder interferometer.

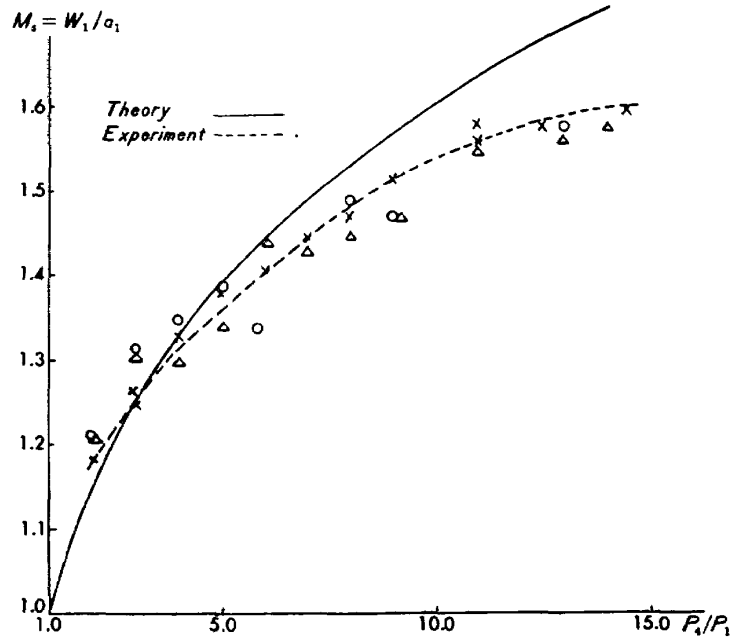

Fig. 17 a. Variation of shock Mach number with initial pressure ratio.

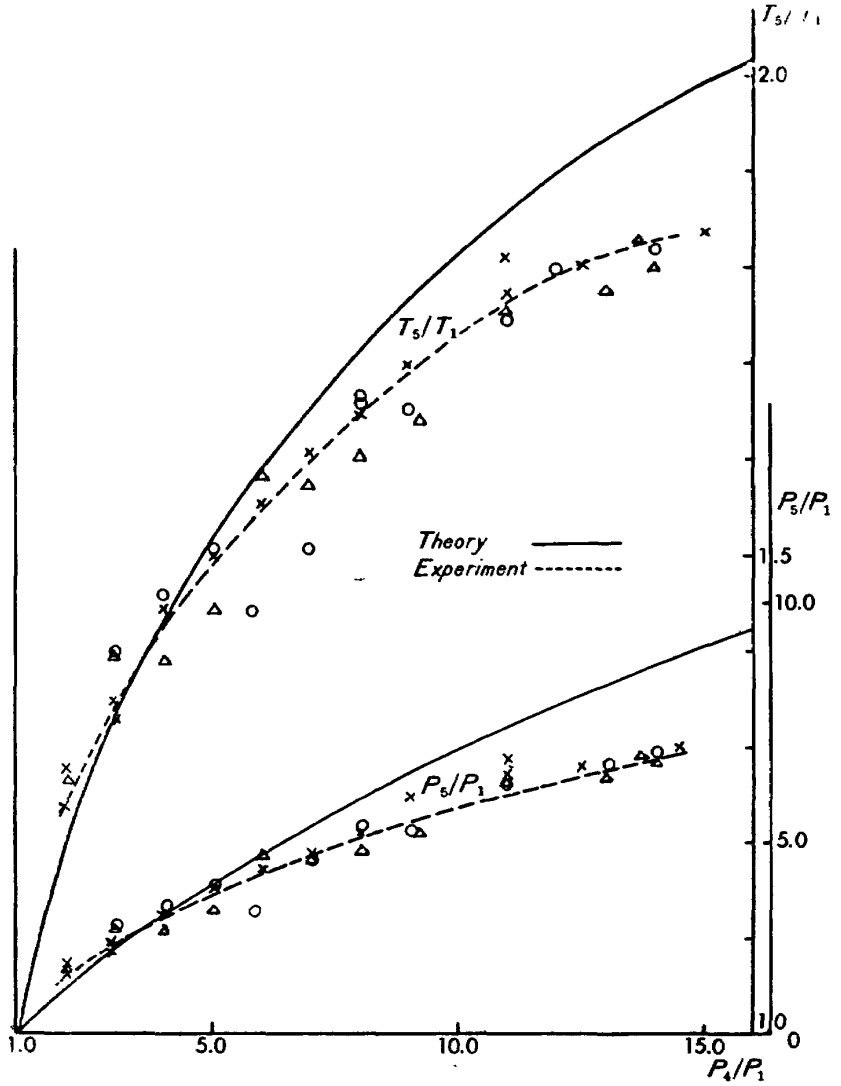

Fig. 17 b. Variation of stagnation pressure and temperature with initial pressure ratio.

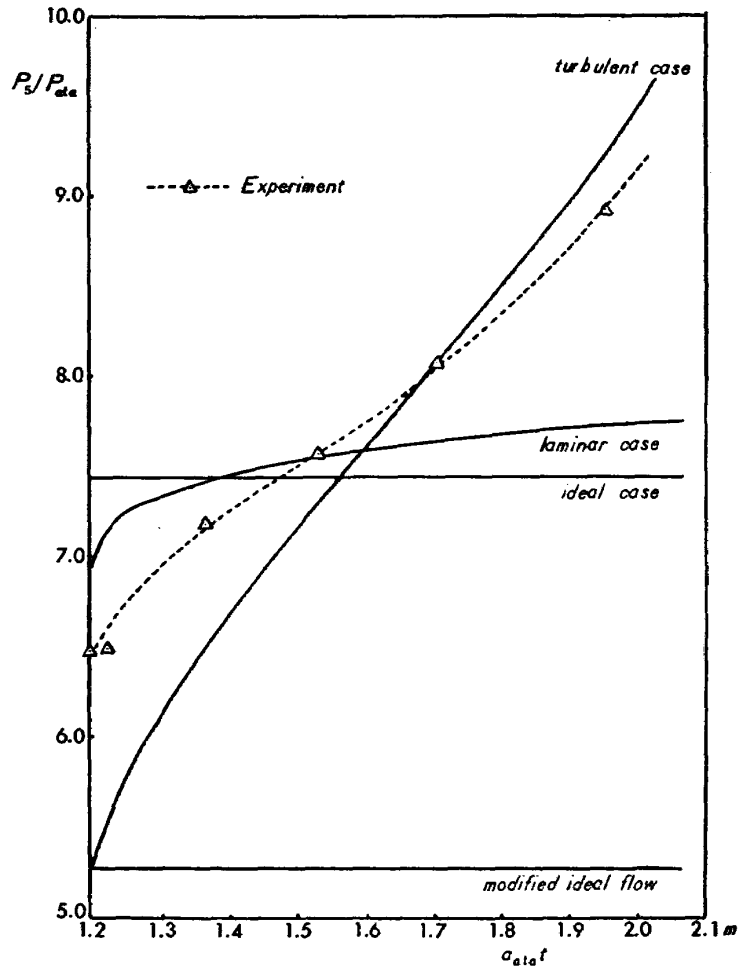

Fig. 18. Variation of stagnation pressure with time.

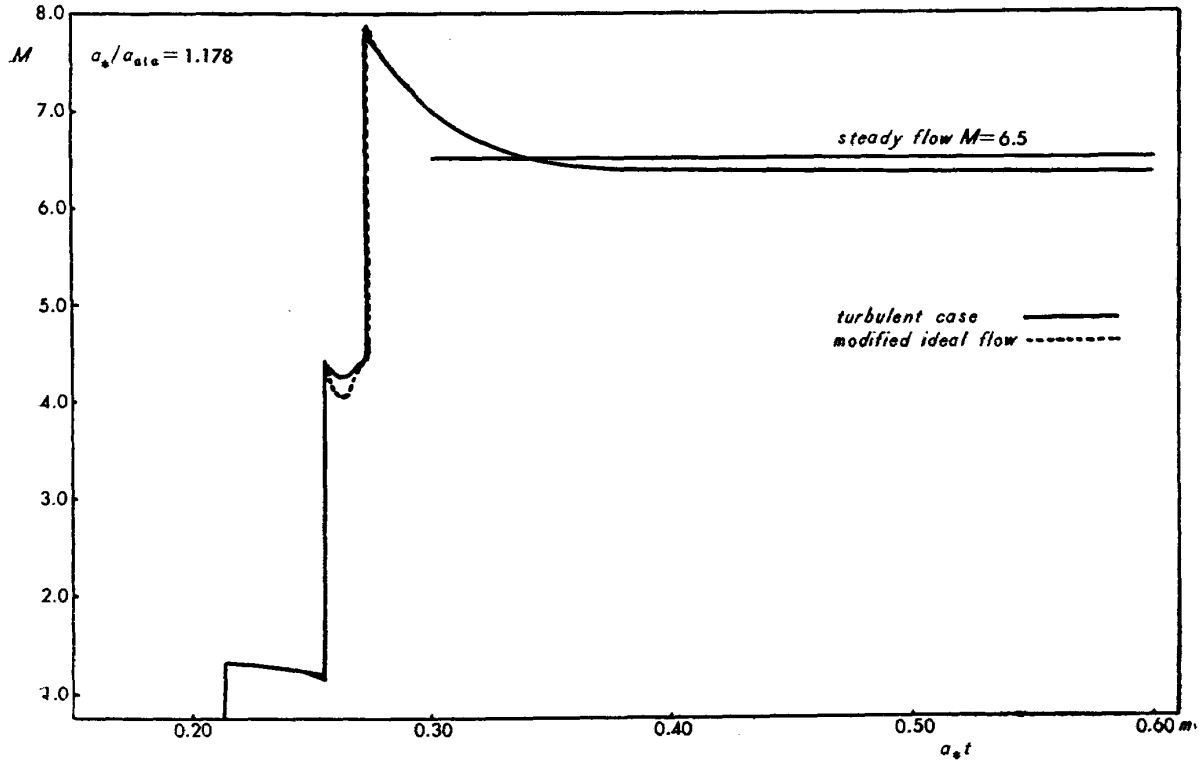

Fig. 19. Variation of Mach number in test section with a_*t.

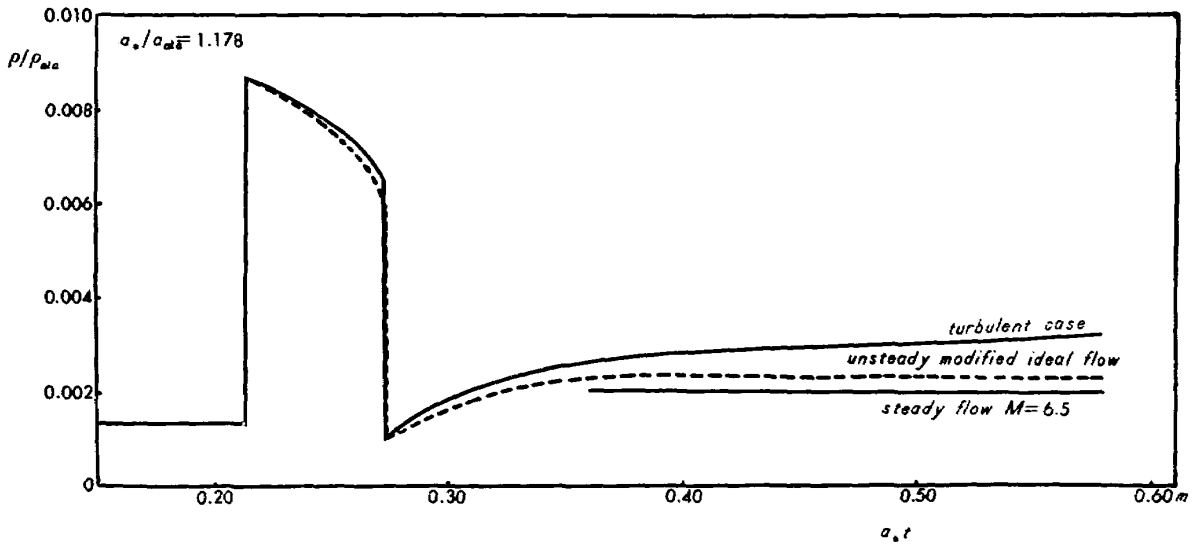

Fig. 20. Variation of pressure in test section with a_*t.

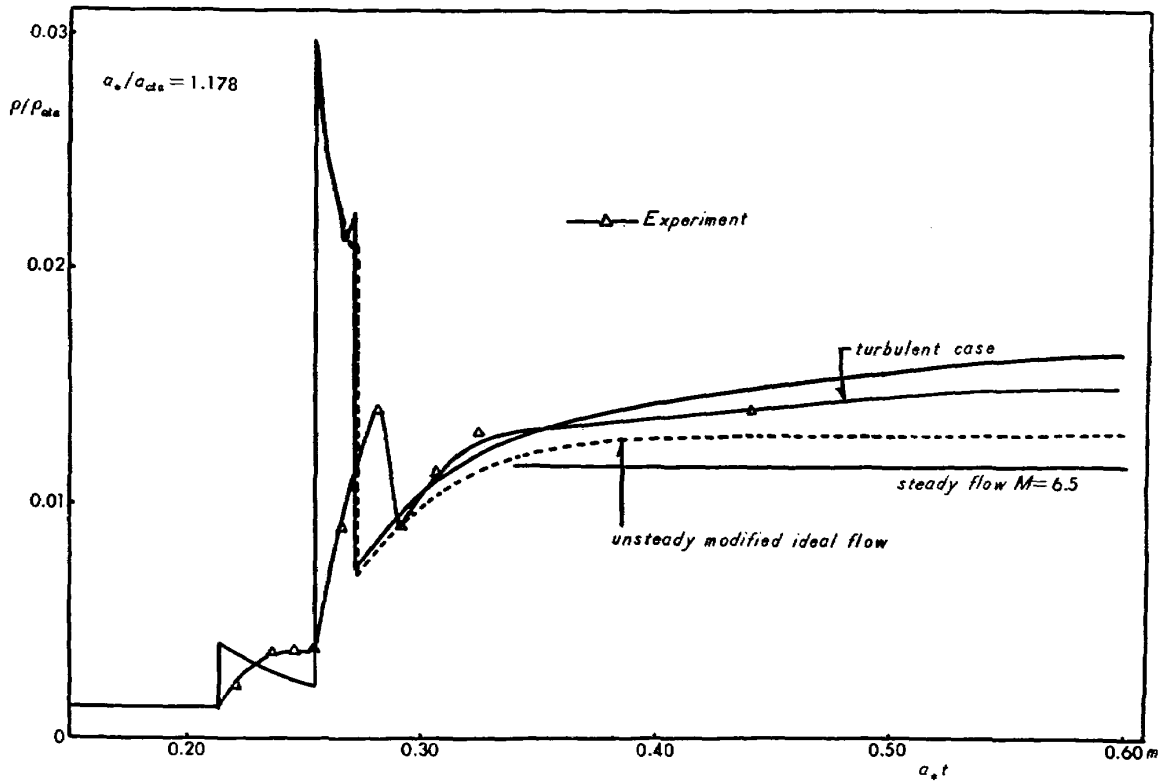

Fig. 21. Variation of density in test section with a_*t.

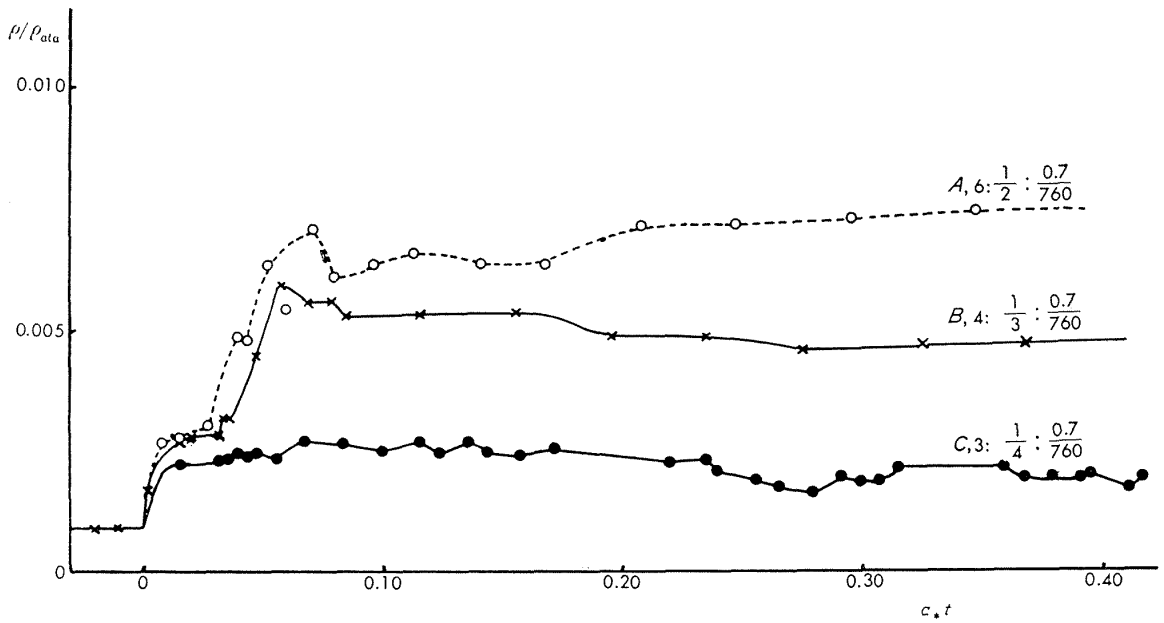

Fig. 22. Variation of density in test section with a_*t.
(Initial pressure; $P_2=6$ ata, $P_1=1/2$ ata, $P_{vac}=0.7$ mmHg
$P_2=4$ ata, $P_1=1/3$ ata, $P_{vac}=0.7$ mmHg
$P_2=3$ ata, $P_1=1/4$ ata, $P_{vac}=0.7$ mmHg)

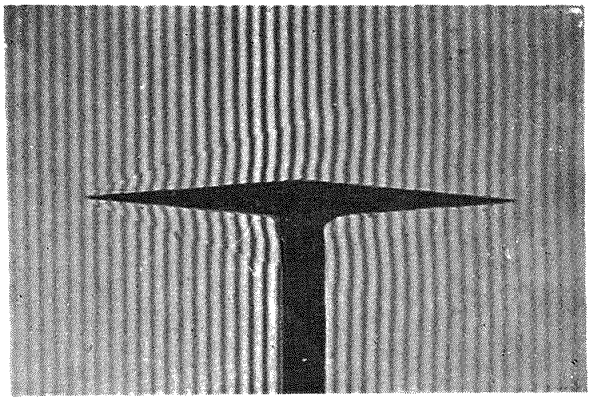

The flow around a double-wedge observed by interferometer.

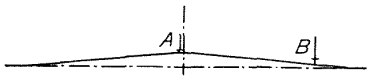

A : $x/c=0.49$ $y/c=0.0415$
B : $=0.91$ $=0.020$

x : distance from the leading edge
y : distance from the surface
c : chord length

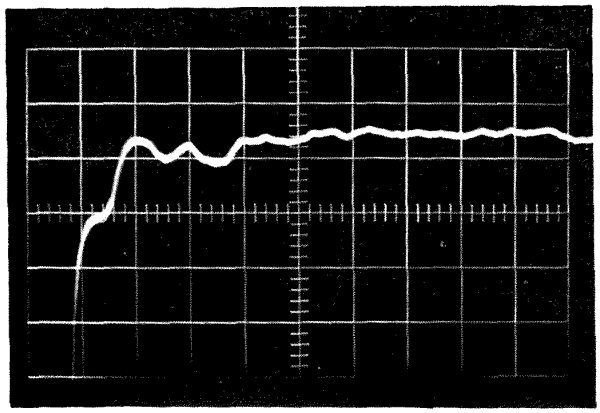

100 μ sec/division 2V/division

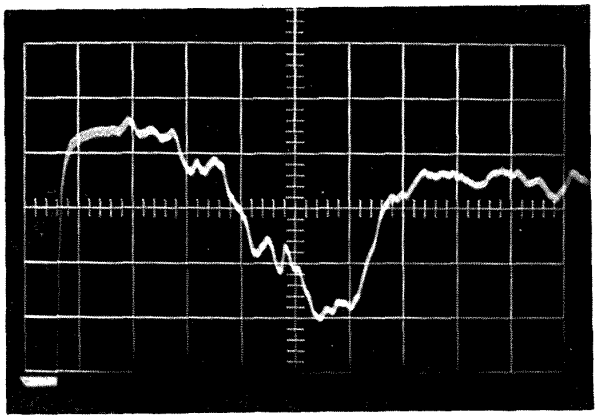

100 μ sec/division 1V/division

Fig. 23. The variation of density near the surface of a double-wedge ($c=0.03$ m).
$P_2=4$ ata, $P_1=1/3$ ata, $P_{vac}=0.7$ mmHg

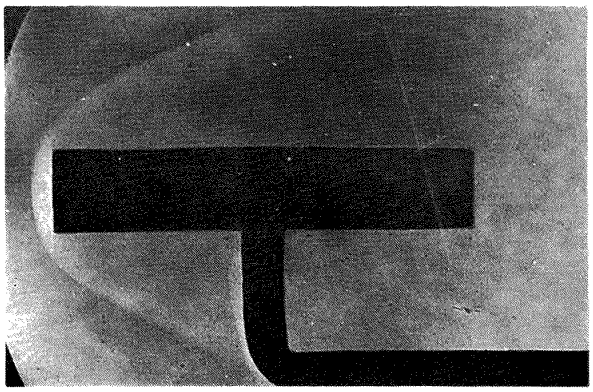

The flow around a flat-nosed cylinder
(0-fringe method)

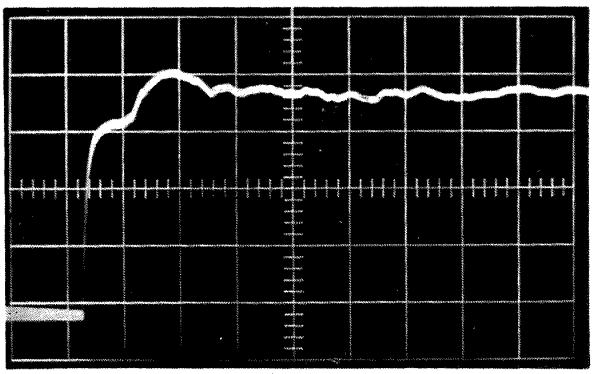

100 μ sec/division 2V/division
Variation of density at A.

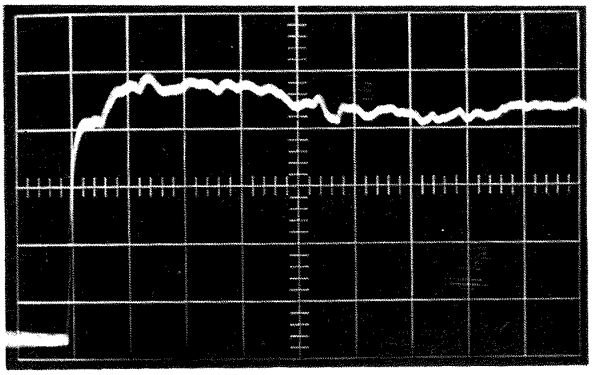

100 μ sec/division 0.5V/division
Variation of density at B.

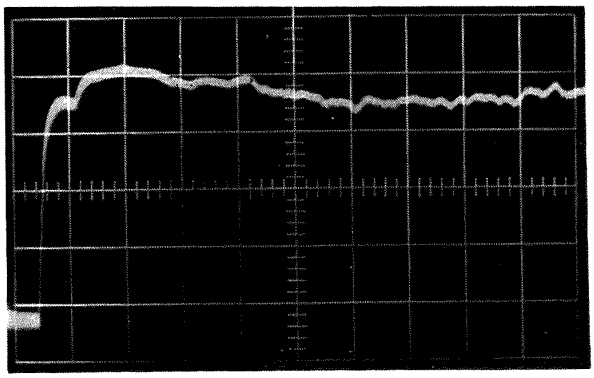

100 μ sec/division 2V/division
Variation of density at C.

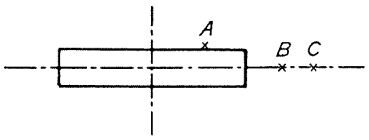

A : $x/D=3.92$ $y/D=0.60$
B : $=6.00$ $=0.00$
C : $=6.00$ $=0.00$

L : length of cylinder
D : Diameter of cylinder
x : distance from the nose of cylinder
y : distance from the axis of cylinder

Fig. 24. The variation of density near the surface of a cylinder ($D=0.01$ m).

$F_2=4$ ata, $P_1=1/3$ ata, $P_{vac}=0.7$ mmHg

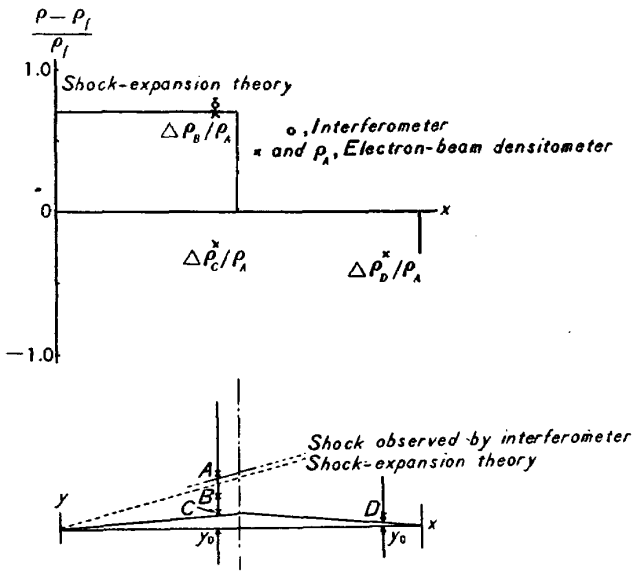

	x/c	$y-y_0/c$
A :	0.44	0.120
B :	0.44	0.049
C :	0.44	0.005
D :	0.91	0.020

Fig. 25. Comparison of the density measured by electron-beam densitometer with the density by interferometer.
(P_2=4 ata, P_1=1/3 ata, P_{vac}=0.6/760 ata)

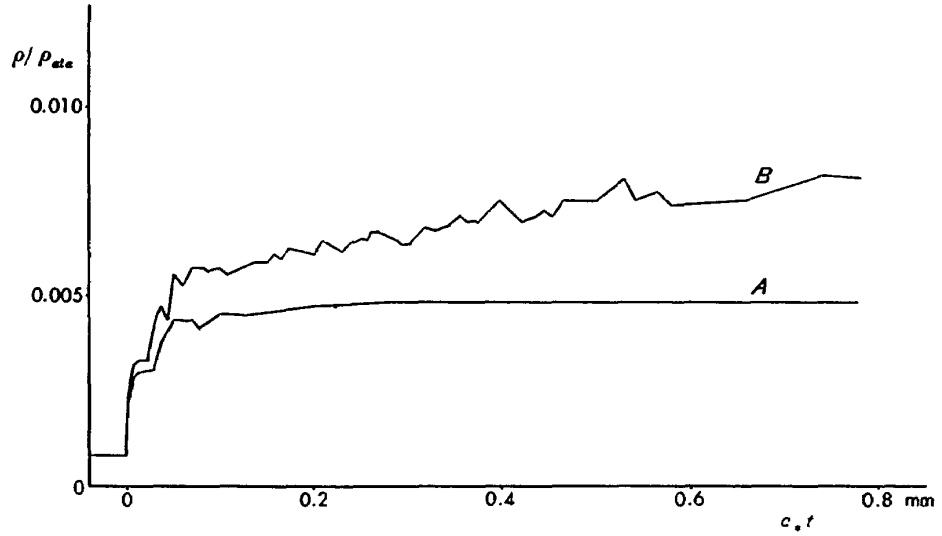

Fig. 26 a. Variation of density with time at A and B.

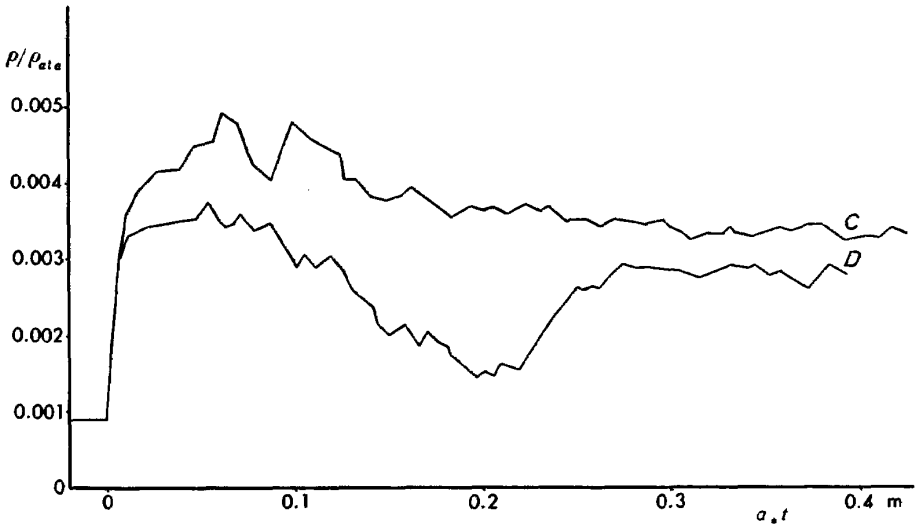

Fig. 26 b. Variation of density with time at C and D.

Table 1. Theoretical conditions of the stagnation and throat.

$P_2/P_1=12$ $P_1=P$ ata, $T_1=T$ ata	P_5/P_1	P_5/P_1	a_5/a_1	u_5/a_1	P_*/P_1	T_*/T_1	a_*/a_1
ideal shock tube theory							
$u_5/a_5=0$	7.931	1.928	1.389	0			
$u_5/a_5=0.0476$	7.441	1.885	1.373	0.0654	3.943	1.573	1.254
modified ideal flow, (turbulent boundary layer case)							
$u_5/a_5=0$	5.983	1.702	1.305	0			
$u_5/a_5=0.0476$	5.271	1.665	1.290	0.0614	2.793	1.388	1.178
$P_2/P_1=14$ ideal shock tube theory							
$u_5/a_5=0$	8.789	2.006	1.416	0			
$u_5/a_5=0.0476$	8.261	1.961	1.400	0.0667	4.378	1.638	1.280
$P_2/P_1=10$ ideal shock tube theory							
$u_5/a_5=0$	7.022	1.838	1.356	0			
$u_5/a_5=0.0476$	6.574	1.797	1.340	0.0638	3.483	1.498	1.224

Appendix A Symbols

The following symbols are used in this paper.

P pressure

$p=\frac{2}{\gamma-1}\left(\frac{P}{P_0}\right)^{\frac{\gamma-1}{2\gamma}}$

a speed of sound

u particle velocity

T temperature

s entropy

$S=e^{\frac{s-s_0}{2C_p}}$

ρ density

M Mach number

W velocity of shock wave

$M_s=W/a_f$ shock Mach number

A cross-sectional area

x, X coordinate parallel to axis of tunnel

t, T time

C_p specific heat at constant pressure

C_v specific heat at constant volume

γ ratio of specific heats
R gas constant
μ molecular weight
α, β coefficients in formula of cross-sectional area change

Subscripts

1~4 regions of shock tube (Fig. 10)
or 1, 2 propagating shock and reflected shock
5 region after reflected shock
0, ata state at the standard atomosphere
vac initial conditions of vacuum chamber
$*$ throat conditions
b conditions behind shock
f conditions ahead of shock
$i, i+1, \ldots.$
$j, j+1, \ldots.$ No. of intersecting point of characteristics
$k, k+1, \ldots.$

Superscripts

q iteration time
$'$ conditions on the way of computing process
$+$ conditions on the back of contact surface
$-$ conditions on the front of contact surface

Symbols in Appendix E, see reference 19)

Appendix B The computing system of the unsteady flow in a divergent nozzle by the method of characteristics

The schematic block diagram of computing system is shown in Fig. B-8. This calculation is classified as follows.

B-I. General equations (3.6)

The initial conditions at $(0,t)$ are given as the following non-dimensional forms,

$$u_{x=0}=u_{x=0}/a_*, \quad p_{x=0}=\frac{2}{\gamma-1}\left(\frac{P_{x=0}}{P_*}\right)^{\frac{\gamma-1}{2\gamma}},$$

$$a_{x=0}=a_{x=0}/a_*, \quad S_{x=0}=e^{\frac{s_{x=0}-s_*}{2\gamma p}}=\frac{a}{a_*}\frac{2}{(\gamma-1)p_{x=0}}$$

where a_0 in equations (3.6) is a_*, the sonic velocity at the throat.

The intersecting point of waves is given by

$$\begin{aligned} x_{i+1}-x_i&=(u_i+a_i)(t_{i+1}-t_i) \\ x_{i+1}-x_j&=(u_j-a_j)(t_{i+1}-t_j) \\ &\rightarrow x_{i+1},\ t_{i+1} \end{aligned} \tag{B.1}$$

The states corresponding to the above point are determined by equations (3.6), that is,

$$\left.\begin{aligned} u_{i+1}-u_i&=-S_i(p_{i+1}-p_i)-a_iu_i\frac{\alpha}{\alpha x_i+\beta}(t_{i+1}-t_i)\\ -(u_{i+1}-u_j)&=-S_j(p_{i+1}-p_i)-a_ju_j\frac{\alpha}{\alpha x_j+\beta}(t_{i+1}-t_i)\end{aligned}\right\} \qquad (B.2)$$

$$(\alpha=0.5382,\quad \beta=0.004)$$

$$\rightarrow u_{i+1},\ p_{i+1}$$

The entropy along the particle velocity u, should be constant,

$$\left.\begin{aligned} X-x_{i+1}&=u_{i+1}(T-t_{i+1})\\ X-x_i/x_i-x_j&=T-t_i/t_i-t_j\end{aligned}\right\} \qquad (B.3)$$

$$S_{i+1}=\frac{X-x_i}{x_i-x_j}(S_i-S_j)+S_i \qquad (B.4)$$

$$\rightarrow S_{i+1}$$

$$a_{i+1}=S_{i+1}\frac{\gamma-1}{2}p_{i+1} \qquad (B.5)$$

$$\rightarrow a_{i+1}$$

Iteration formula;

$$u_i^{q+1}=\frac{u_i^q+u_{i+1}^q}{2} \qquad a_i^{q+1}=\frac{a_i^q+a_{i+1}^q}{2}$$

$$u_j^{q+1}=\frac{u_j^q+u_{i+1}^q}{2} \qquad a_j^{q+1}=\frac{a_j^q+a_{i+1}^q}{2}$$

$$\vdots \qquad\qquad \vdots$$

$$|u_i^{q+1}-u_i^q|<\varepsilon \quad , \quad |u_j^{q+1}-u_j^q|<\varepsilon$$

$$|a_i^{q+1}-a_i^q|<\varepsilon \quad , \quad |a_j^{q+1}-a_j^q|<\varepsilon$$

$$|u_i^{q+1}-u_i^q|<\varepsilon \quad , \quad |a_i^{q+1}-a_{i+1}^q|<\varepsilon$$

$$\varepsilon=1\times10^{-5}$$

The iteration process is repeated till $\varepsilon=1\times10^{-5}$, and x_{i+1}, t_{i+1}, a_{i+1}, p_{i+1}, u_{i+1}, $e^{\frac{S_{i+1}-S_i}{2Cp}}$ are determined.

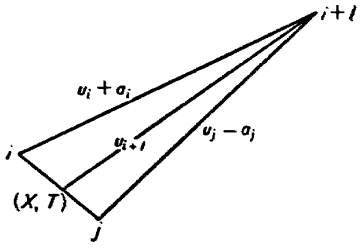

Fig. B-I.

The computed states are stored in memory for the calculation of states along the next Mach line from the initial condition at the throat to the first shock.

B-II First shock

$$\left.\begin{aligned} x_{i+1}-x_i&=(u_i+a_i)(t_{i+1}-t_i)\\ x_{i+1}-x_j&=W_j(t_{i+1}-t_j)\end{aligned}\right\} \qquad (B.6)$$

$$\rightarrow x_{i+1},\ t_{i+1}$$

The shock conditions corresponding to the above point are determined from the characteristic equations along $u+a$ (in eqs. (3.6)) and the shock relations.

$$\left.\begin{aligned} u_{i+1}-u_i&=-S_i(p_{i+1}-p_i)-a_iu_i\frac{\alpha}{\alpha x+\beta}(t_{i+1}-t_i)\\ u_{i+1}&=\frac{\dfrac{a_{vac}}{a_*}\left\{\left(\dfrac{\gamma-1}{2}p_{i+1}\right)^{\frac{2\gamma}{\gamma-1}}\dfrac{P_*}{P_{vac}}-1\right\}}{\gamma\left[\dfrac{\gamma-1}{2\gamma}\left\{\dfrac{\gamma+1}{\gamma-1}\left(\dfrac{\gamma-1}{2}p_{i+1}\right)^{\frac{\gamma-1}{2\gamma}}\dfrac{P_*}{P_{vac}}+1\right\}\right]^{1/2}}\end{aligned}\right\} \qquad (B.7)$$

$$P_*/P_{vac}=760\times 2.793$$

$$a_*/a_{vac}=1.178$$

$$\rightarrow u_{i+1},\ p_{i+1}$$

$$P/P_{vac}=\left(\frac{\gamma-1}{2}p_{i+1}\right)^{\frac{\gamma-1}{2\gamma}}\frac{P_*}{P_{vac}} \tag{B.8}$$

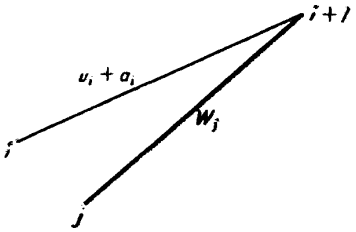

Fig. B-2.

$$W_{j+1}=\frac{a_*}{a_{vac}}\left\{\frac{2\gamma}{\gamma-1}\left[\left(\frac{\gamma-1}{\gamma+1}\right)\frac{P}{P_{vac}}+1\right]\right\}^{1/2} \tag{B.9}$$

$$a_{j+1}=\frac{a_*}{a_{vac}}\left\{\frac{\frac{P}{P_{vac}}\left(\frac{\gamma-1}{\gamma+1}+\frac{P}{P_{vac}}\right)}{1+\frac{\gamma+1}{\gamma-1}\frac{P}{P_{vac}}}\right\}^{1/2} \tag{B.10}$$

$$S_{j+1}=e^{\frac{s_{j+1}-s_*}{2Cp}}=a_{j+1}\frac{2}{(\gamma-1)p_{j+1}} \tag{B.11}$$

Iteration; see section B–I

B-III Contact surface

$$\left.\begin{aligned}x_{ij}-x_i&=(u_i+a_i)(t_{ij}-t_i)\\x_{ij}-x_j&=u_j(t_{ij}-t_j)\end{aligned}\right\} \tag{B.12}$$

$$\left.\begin{aligned}x_{jk}-x_j&=u_j(t_{jk}-t_j)\\x_{jk}-x_k&=(u_k-a_k)(t_{jk}-t_k)\end{aligned}\right\} \tag{B.13}$$

(a) $x_{ij}-x_{jk}>0$

$$\left.\begin{aligned}u_{x=X}-u_j&=(u_i-u_j)\frac{X-x_j}{x_i-x_j}\\a_{x=X}-a_j^+&=(a_i-a_j)\frac{X-x_j}{x_i-x_j}\\p_{x=X}-p_j&=(p_i-p_j)\frac{X-x_j}{x_i-x_j}\\S_{x=X}&=a_{x=X}\frac{2}{(\gamma-1)p_{x=X}}\end{aligned}\right\} \tag{B.14}$$

$$u_{x=X},\ p_{x=X},\ p_k,\ u_k\rightarrow \text{Eq. (B.2)}\ \&\ \frac{a_{jk}^+}{a_{jk}^-}=\text{Const.}$$

$$\rightarrow u_{jk},\ p_{jk},\ a_{jk}^+,\ a_{jk}^-,\ S_{jk}$$

Iteration; see section B–I

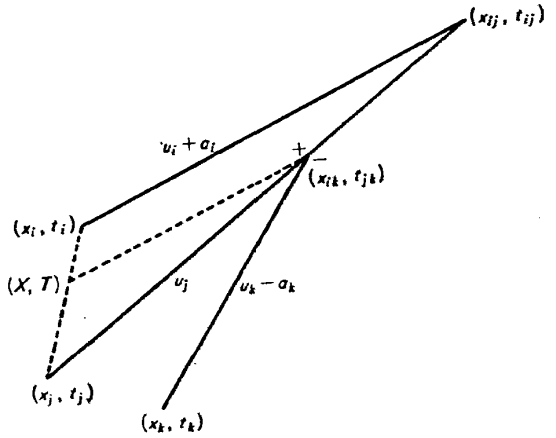

Fig. B-3.

(b) $x_{jk}-x_{ik}<0$

$$\left.\begin{aligned} u_{x=X'}-u_j&=(u_k-u_j)\frac{X'-x_k}{x_j-x_k}\\ a_{x=X'}-a_j^-&=(u_k-u_j)\frac{X'-x_k}{x_j-x_k}\\ p_{x=X'}-p_j&=(u_k-u_j)\frac{X'-x_k}{x_j-x_k}\end{aligned}\right\} \qquad \text{(B. 15)}$$

$$u_{x=X'},\ p_{x=X'},\ u_k,\ p_k$$

$$\rightarrow \text{Eq. (B.2)} \ \&\ \frac{a_{ij}^+}{a_{ij}^-}=\text{Const.}$$

$$\rightarrow u_{ij},\ p_{ij},\ a_{ij}^+,\ a_{ij}^-,\ S_{ij}$$

Iteration; see section B-I

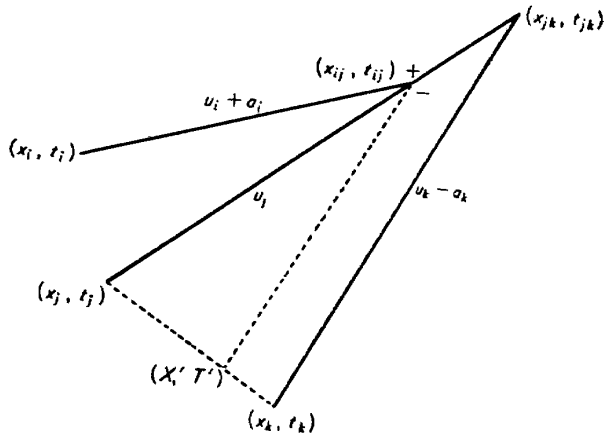

Fig. B-4.

B-IV Secondary shock

(1)

$$\left.\begin{aligned} x_{k+1}-x_j&=(u_j-a_j)(t_{k+1}-t_j)\\ x_{k+1}-x_k&=(u_k-a_k)(t_{k+1}-t_k)\end{aligned}\right\} \qquad \text{(B. 16)}$$

$$\rightarrow x_{k+1},\ t_{k+1}$$

$$x_i, t_i, x_j, t_j \rightarrow \text{Eq. (B.1)} \rightarrow x_{i+1},\ t_{i+1}$$

In the case of $x_j-x_k>0$, $x_k-x_{k+1}>0$, and $x_{i+1}-x_{k+1}<0$,

$$\left.\begin{aligned} u_{k+1}&=u_k-(u_{i+1}-u_k)\frac{x_{k+1}-x_j}{x_{i+1}-x_j}\\ p_{k+1}&=p_k-(p_{i+1}-p_k)\frac{x_{k+1}-x_j}{x_{i+1}-x_j}\\ a_{k+1}&=a_k-(a_{i+1}-a_k)\frac{x_{k+1}-x_j}{x_{i+1}-x_j}\\ S_{k+1}&=S_k-(S_{i+1}-S_k)\frac{x_{k+1}-x_j}{x_{i+1}-x_j}\end{aligned}\right\} \qquad \text{(B. 17)}$$

$$\left.\begin{aligned}\frac{u_{b(k+1)}}{a_{k+1}}-u_{k+1}\frac{a_*}{a_{k+1}}&=\frac{\left\{\left(\frac{p_{b(k+1)}}{p_{k+1}}\right)^{\frac{2\gamma}{\gamma-1}}-1\right\}}{\gamma\left[\frac{\gamma-1}{2\gamma}\left\{\frac{\gamma+1}{\gamma-1}\left(\frac{p_{b(k+1)}}{p_{k+1}}\right)^{\frac{2\gamma}{\gamma-1}}+1\right\}\right]^{1/2}}\\ -(u_{b(k+1)}-u_k)&=-S_k(p_{b(k+1)}-p_k)-a_ku_k\frac{\alpha}{\alpha x_k+\beta}\end{aligned}\right\}\qquad\text{(B.18)}$$

$$\rightarrow u_{b(k+1)},\ p_{b(k+1)}$$

$$\frac{p_{b(k+1)}}{p_{k+1}}\rightarrow P=\left(\frac{p_{b(k+1)}}{p_{k+1}}\right)^{\frac{2\gamma}{\gamma-1}}\qquad\text{(B.19)}$$

$$a_{b(k+1)}=a_{k+1}\left\{P\left(\frac{\gamma+1}{\gamma-1}+P\right)\Big/1+\frac{\gamma+1}{\gamma-1}P\right\}^{1/2}\qquad\text{(B.20)}$$

$$S_{b(k+1)}=a_{b(k+1)}\frac{2}{(\gamma-1)p_{b(k+1)}}\qquad\text{(B.21)}$$

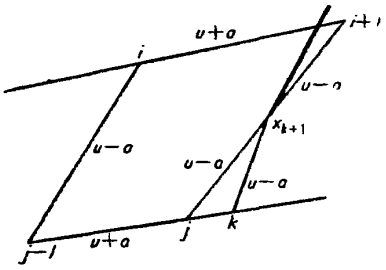

Fig. B-5.

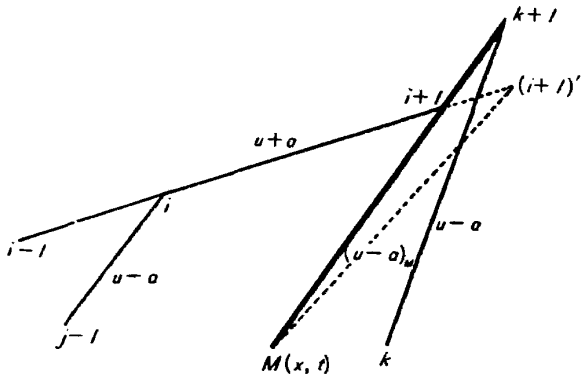

Fig. B-6.

(2)

$$\left.\begin{aligned}x_{i+1}-x_i&=(u_i+a_i)(t_{i+1}-t_i)\\ x_{i+1}-x_M&=(M-a_{Mf})(t_{i+1}-t_M)\\ x_{k+1}-x_M&=(M-a_{Mf})(t_{k+1}-t_M)\\ x_{k+1}-x_k&=(u_k-a_k)(t_{k+1}-t_k)\end{aligned}\right\}\qquad\text{(B.22)}$$

$x_{i+1}-x_{k+1}<0$,

u, p, a, S at $M(x,t)\rightarrow$ Eqs. (B.1) & (B.2)

$$\rightarrow x'_{i+1},\ t'_{i+1},\ u'_{i+1},\ p'_{i+1},\ a'_{i+1}$$

$$\left.\begin{aligned}u_{i+1}&=u_i+(u'_{i+1}-u_i)\frac{x_{i+1}-x_i}{x'_{i+1}-x_i}\\ p_{i+1}&=p_i+(p'_{i+1}-p_i)\frac{x_{i+1}-x_i}{x'_{i+1}-x_i}\end{aligned}\right\}\qquad\text{(B.23)}$$

$S_{i+1}\rightarrow$ Eqs. (B.3) & (B.4)

$a_{i+1}\rightarrow$ Eq. (B.5)

$M_{i+1}=M$

$$\frac{p_{b(i+1)}}{p_{i+1}}=\frac{p_{b(x=M)}}{p_{x=M}}$$

$\frac{p_{b(i+1)}}{p_{i+1}}\rightarrow$ Eq. (B.19) $\rightarrow$ Eqs. (B.20), (B.21), the first eq. of (B.18)

$$\rightarrow a_{b(i+1)},\ S_{b(i+1)},\ u_{b(i+1)}$$

(3)

$$x_{i+1}-x_{k+1}>0$$

$$\left.\begin{aligned} X-x_{k+1}&=(u_{i+1}-a_{i+1})(T-t_{k+1})\\ X-x_i&=(T-t_i)\frac{x_{i+1}-x_i}{t_{i+1}-t_i}\end{aligned}\right\} \tag{B.24}$$

$$\left.\begin{aligned} X'-x_{k+1}&=(u_{i+1}+a_{i+1})(T'-t_{k+1})\\ X'-x_{j-1}&=(T'-t_{j-1})\frac{x_i-x_{j-1}}{t_i-t_{j-1}}\end{aligned}\right\} \tag{B.25}$$

$u,\ p,\ a\ S$ at $M(x,\ t)\rightarrow$ Eqs. (B.1) & (B.2)

$\rightarrow x'_{i+1},\ t'_{i+1},\ u'_{i+1},\ p'_{i+1},\ a'_{i+1}\rightarrow$ Eq. (B.23)

$\rightarrow u_{i+1},\ p_{i+1},\ a_{i+1},\ S_{i+1}\rightarrow$ Eq. (B.23) $\begin{cases} i+1=k+1\\ (i+1)'=i+1\\ i=M\end{cases}$

$\rightarrow u_{k+1},\ p_{k+1},\ a_{k+1},\ S_{k+1}\rightarrow$ Eq. (B.18) $\rightarrow u_{b(k+1)},\ p_{b(k+1)}$

$\dfrac{p_{b(k+1)}}{p_{k+1}}\rightarrow$ Eqs. (B.20) & (B.21) $\rightarrow a_{b(k+1)},\ S_{b(k+1)}$

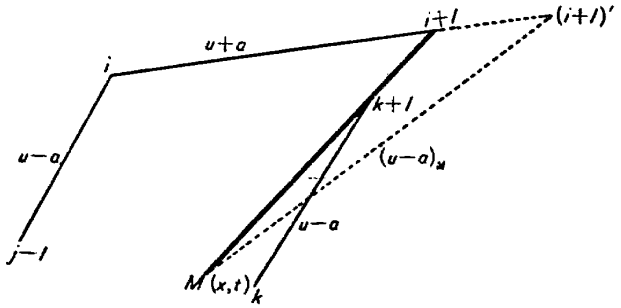

Fig. B-7.

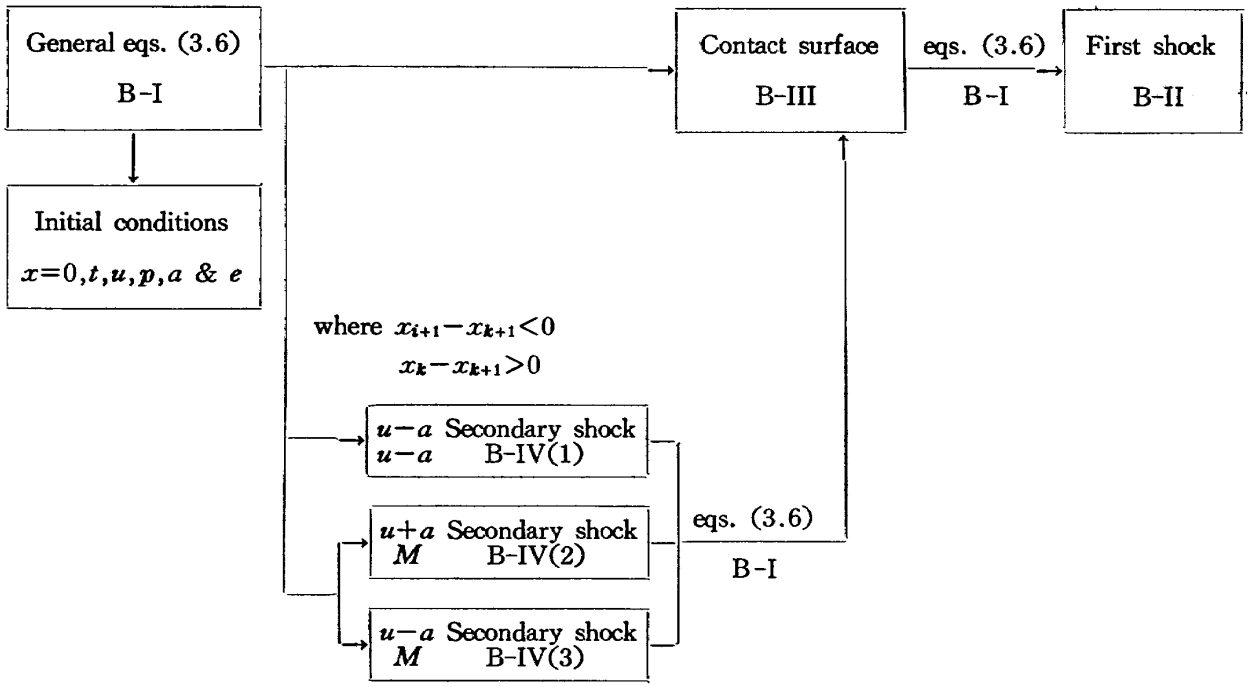

Fig. B-8. Block diagram of computing system.

Appendix C-I, Computing process of Region 5

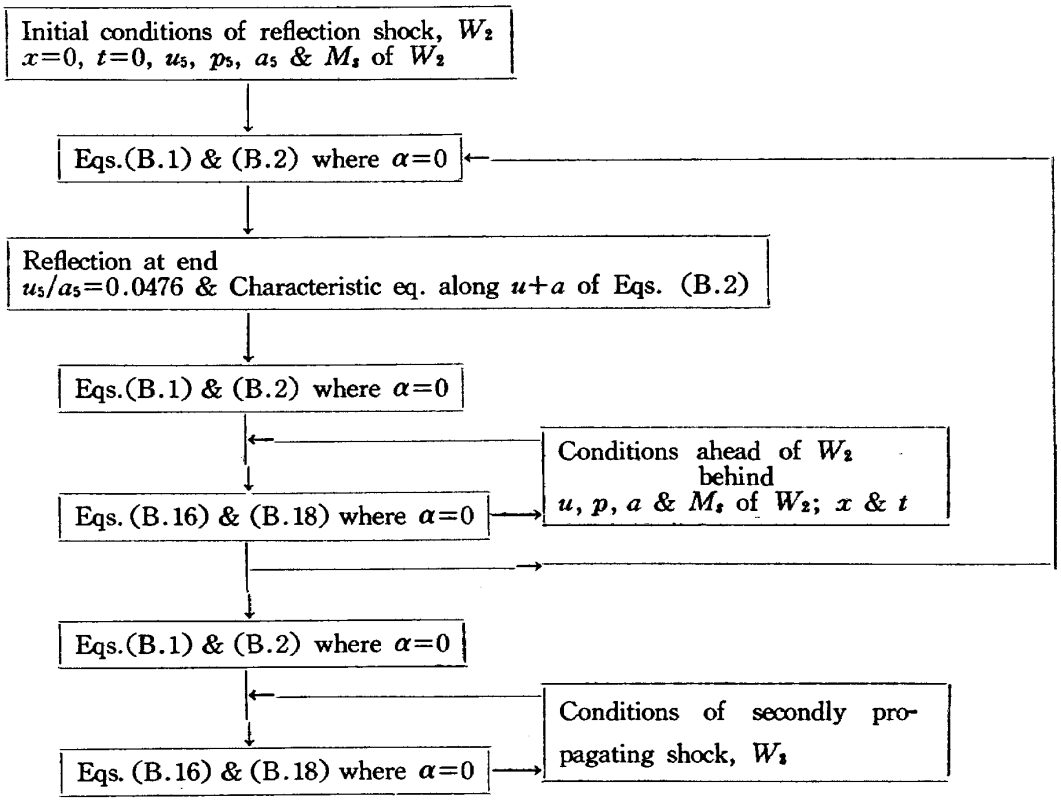

see Fig. 11.

C-II, Computing process of throat

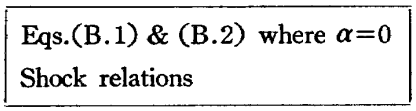

see Fig. 12.

Appendix D Piezo-electric pressure gauge 7)

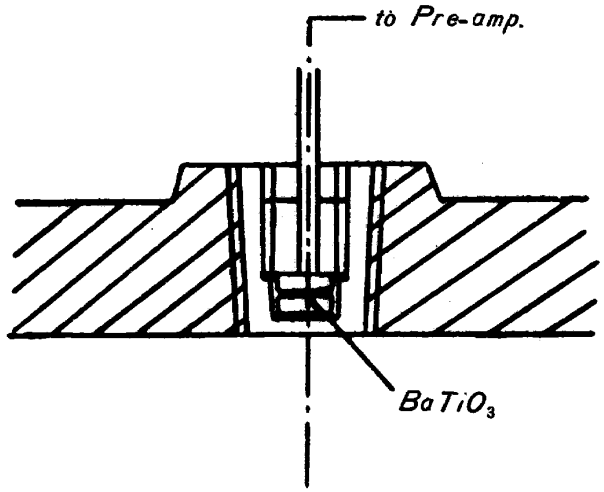

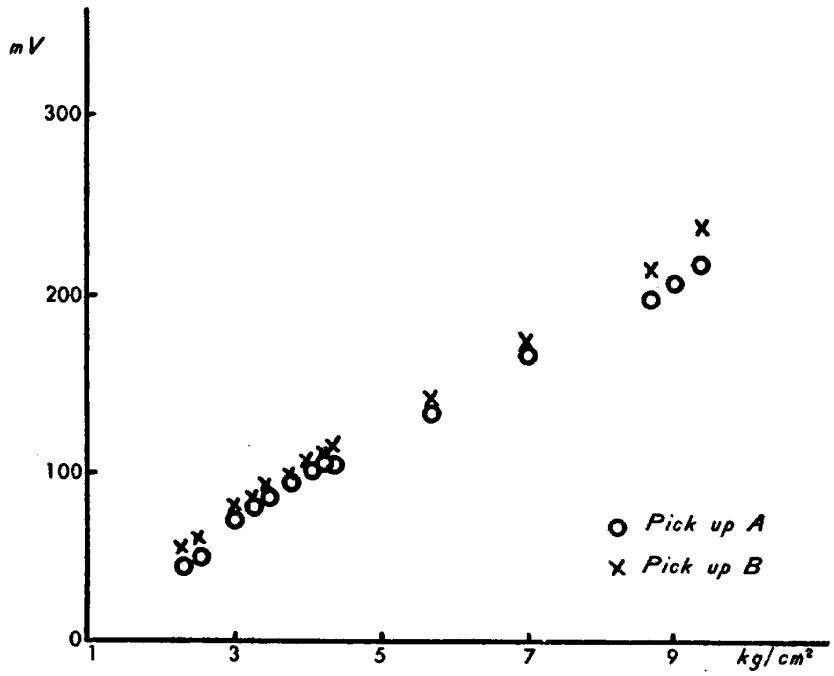

Fig. D-I. Piezo-electric pressure gauge (barium titanate).

Appendix E. The attenuation of shock wave by the effect of boundary layer behind it[19]

In the ideal shock tube theory, the following shock relations are used

$$\left.\begin{aligned}\frac{p_2}{p_1}&=\frac{2\gamma M_s^2-(\gamma-1)}{\gamma+1}\\ \frac{u_2}{a_1}&=\frac{2}{\gamma+1}\frac{M_s^2-1}{M_s}\\ \frac{\rho_2}{\rho_1}&=\frac{(\gamma+1)M_s^2}{(\gamma-1)M_s^2+2}\end{aligned}\right\} \tag{E.1}$$

where $M_s=W/a_1$ is the shock Mach number. If the shock is perturbed, conditions directly behind the shock (designed by subscript 2,0) can be expressed as

$$\left.\begin{aligned}\frac{\Delta p_{2,0}}{p_2}&=\frac{4\gamma M_s^2}{2\gamma M_s^2-(\gamma-1)}\frac{\Delta M_s}{M_s}\\ \frac{\Delta u_{2,0}}{u_2}&=\frac{2\gamma M_s^2-(\gamma-1)}{4\gamma M_s^2}\frac{M_s^2+1}{M_s^2-1}\frac{\Delta p_{2,0}}{p_2}\\ \frac{\Delta \rho_{2,0}}{\rho_2}&=\frac{2\gamma M_s^2-(\gamma-1)}{\gamma M_s^2\{(\gamma-1)M_s^2+2\}}\frac{\Delta p_{2,0}}{p_2}\\ \frac{\Delta T_{2,0}}{T_2}&=\frac{\Delta p_{2,0}}{p_2}-\frac{\Delta \rho_{2,0}}{\rho_2},\quad \frac{\Delta S_{2,0}}{Cv}=\frac{\Delta p_{2,0}}{p_2}-\gamma\frac{\Delta \rho_{2,0}}{\rho_2}\end{aligned}\right\} \tag{E.2}$$

where $\Delta S_{2,0}$ is the entropy perturbation.

Under the assumptions that the boundary layer is wholly laminar or wholly turbulent ($n_3=n_2=n$), the two pressure disturbance which are shown in Fig. E 1, become

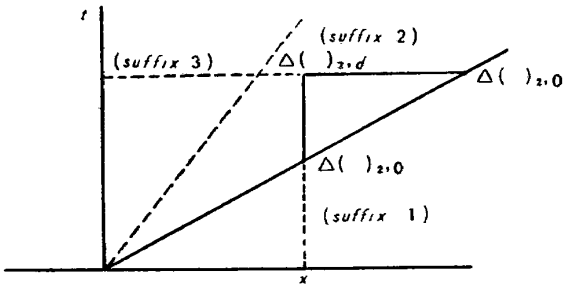

Fig. E-I.

$$\left.\begin{aligned}&-\frac{\Delta p_2^+,_d}{p_2}\left(\frac{d}{u_s t}\right)^{1-n}\left(\frac{a_2 d}{\nu_2}\right)^n\frac{1-n}{2\gamma L_2(M_2^2)^{1-n}}\\ &=\left(\frac{1}{1+M_2-\frac{u_s}{a_2}}+\frac{C}{1-M_2+\frac{u_s}{a_2}}-\frac{D\gamma L_{32}(\nu_{32})^n a_{23}}{1+M_3+a_{43}}\right)\\ &\qquad\times\left\{(1+M_2)\frac{a_2}{u_s}-\frac{x}{u_s t}\right\}^{1-n}\\ &-\frac{1}{1+M_2-\frac{u_s}{a_2}}\left(\frac{1-\frac{x}{u_s t}}{\frac{u_s}{a_2}-M_2}\right)^{1-n}\end{aligned}\right\} \tag{E.3}$$

and

$$
\left.
\begin{aligned}
&-\frac{\Delta p_2^-, d}{p_2}\left(\frac{d}{u_s t}\right)^{1-n}\left(\frac{a_2 d}{\nu_2}\right)^n \frac{1-n}{2\gamma L_2 (M_2^2)^{1-n}} \\
&= \frac{1}{1-M_2+\dfrac{u_s}{a_2}}\left(\frac{1-\dfrac{x}{u_s t}}{\dfrac{u_s}{a_2}-M_2}\right)^{1-n} \\
&\quad + E\left\{\frac{1}{1+M_2-\dfrac{u_s}{a_2}} + \frac{C}{1-M_2+\dfrac{u_s}{a_2}} - \frac{D\gamma L_{32}(\nu_{32})^n a_{23}}{1+M_3+a_{43}}\right\} \\
&\quad \times\left(\frac{1+M_2-\dfrac{u_s}{a_2}}{1-M_2+\dfrac{u_s}{a_2}}\right)^{1-n}\left\{(1-M_2)\frac{a_2}{u_s}+\frac{x}{u_s t}\right\}^{1-n}
\end{aligned}
\right|
$$

The complete pressure and velocity perturbation at point d are obtained from the above equations (A 3) according to

$$
\left.
\begin{aligned}
\Delta p_2, d &= \Delta p_2^+, d + \Delta p_2^-, d \\
\Delta u_2, d &= \frac{1}{\rho_2 a_2}(\Delta p_2^+, d - \Delta p_2^-, d)
\end{aligned}
\right\} \qquad \text{(E.4)}
$$

For wholly laminar boundary layer case $n=1/2$, and for wholly turbulent boundary layer case $n=1/5$.

NAL TR-37T

NATIONAL AERONAUTICAL LABORATORY

Studies of the Flow in a Low Pressure Hypersonic Shock Tunnel Using an Electron-Beam Densitometer

January, 1963 p. 33

The flow of a hypersonic shock tunnel using a double diaphragm is analysed by the method of characteristics in consideration of the growth of the boundary layer in the shock tube and compared with the experimental results measured by an electron-beam densitometer. The density in the test section increases with time according to the boundary layer growth in the medium pressure channel of the shock tunnel and is compared with the computed results of the unsteady flow theory. Some criteria on the effect of the boundary layer and the establishment of the hypersonic flow are given. The density in the boundary layer on a body at a hypersonic speed is also measured by the densitometer.

I. Isamu WADA

II. NAL TR-37T

III. 533.6.011.55
533.6.071.8
533.6.08

NAL TR-37T

NATIONAL AERONAUTICAL LABORATORY

Studies of the Flow in a Low Pressure Hypersonic Shock Tunnel Using an Electron-Beam Densitometer

January, 1963 p. 33

The flow of a hypersonic shock tunnel using a double diaphragm is analysed by the method of characteristics in consideration of the growth of the boundary layer in the shock tube and compared with the experimental results measured by an electron-beam densitometer. The density in the test section increases with time according to the boundary layer growth in the medium pressure channel of the shock tunnel and is compared with the computed results of the unsteady flow theory. Some criteria on the effect of the boundary layer and the establishment of the hypersonic flow are given. The density in the boundary layer on a body at a hypersonic speed is also measured by the densitometer.

I. Isamu WADA

II. NAL TR-37T

III. 533.6.011.55
533.6.071.8
533.6.08

NAL TR-37T

NATIONAL AERONAUTIBAL LABORATORY

Studies of the Flow in a Low Pressure Hypersonic Shock Tunnel Using an Electron-Beam Densitometer

January, 1963 p. 33

The flow of a hypersonic shock tunnel using a double diaphragm is analysed by the method of characteristics in consideration of the growth of the boundary layer in the shock tube and compared with the experimental results measured by an electron-beam densitometer. The density in the test section increases with time according to the boundary layer growth in the medium pressure channel of the shock tunnel and is compared with the computed results of the unsteady flow theory. Some criteria on the effect of the boundary layer and the establishment of the hypersonic flow are given. The density in the boundary layer on a body at a hypersonic speed is also measured by the densitometer.

I. Isamu WADA

II. NAL TR-37T

III. 533.6.011.55
533.6.071.8
533.6.08

TR-26	Preliminary Tests of Supersonic Nozzles for the Supersonic Blow-down Wind Tunnel	Toshio KAWASAKI, Yujiro OKABE, Yoshikazu OGATA & Hisashi AADO	Mar. 1962
TR-27	An Approximate Analysis for Unsteady Transonic Flow	Iwao HOSOKAWA & Hajime MIYOSHI	July 1962
TR-28	On Fatigue Cracks	Yukihiko TAKENAKA	Aug. 1962
TR-29	On the Design and Construction of 1 m×1 m Supersonic Blowdown Wind Tunnel	The Staff of the Second Aerodynamics Division	Sept. 1962
TR-30	On the Natural Vibration of Plate-Like Wings	Tadahiko KAWAI, Taketoshi HANAWA, Hayato TOGAWA, Toshiyuki TAKAHASH & Shinishi KOSHIIDE	Sept. 1962
TR-31	On the Instability and Small Natural Torsional Vibration of a Thin Wing under a Thermal Stress	Tadahiko KAWAI, Yoichi HAYASHI Hayato TOGAWA	Nov. 1962
TR-32	A Method of Analysis on the Compressive Strength of Stiffened Plates	Tadahiko KAWAI & Koichi EGAWA	Nov. 1962
TR-33	Repeated Load Testing Rigs for Full-Scale Aircraft Wing Structures	Kazuyuki TAKEUCHI, Koichi ONO & Soshiro IIDA	Dec. 1962
TR-34	An Investigation of High Speed Axial Flow Compressor (I) Studies on Aerofoils and Cascades	Masakatsu MATSUKI, Koichi OYAMA & Toshio MIYACHI	Jan. 1963
TR-35	An Investigation of High Speed Axial Flow Compressor (II) Design and Overall Performance of a Single Stage Axial Flow Compressor	Masakatsu MATSUKI, Koshio MIYACHI, Koichi OYAMA, Akira YOSHIDA, Hideo NISHIWAKI & Tadasuke IWABU	Jan. 1963
TR-36	Studies of Surface Heat Transfer Using a Hypersonic Shock Tunnel	Isamu WADA & Riichi MATSUZAKI	Feb. 1963

TECHNICAL REPORT OF NATIONAL AERONAUTICAL LABORATORY
TR-37T

航空技術研究所報告37号（欧文）

昭和38年3月 発行

発行所 航空技術研究所
東京都三鷹市新川700
電話武蔵野(0422)(3)5171(代表)

印刷所 笠井出版印刷社
東京都港区芝南佐久間町1の53

Published by
NATIONAL AERONAUTICAL LABORATORY
700, Shinkawa, Mitaka, Tokyo
JAPAN